Water-Rock Interactions, Ore Deposits, and Environmental Geochemistry: A Tribute to David A. Crerar
© The Geochemical Society, Special Publication No. 7, 2002
Editors: Roland Hellmann and Scott A. Wood

Experimental pressure solution compaction of chalk in aqueous solutions. Part 2. Deformation examined by SEM, porosimetry, synthetic permeability, and X-ray computerized tomography

Roland Hellmann[1*], Patrick Gaviglio[2], Peter J.N. Renders[1**],
Jean-Pierre Gratier[1], Samir Békri[3 ***], Pierre Adler[3]

[1]Crustal Fluids and Dynamics Group, LGIT, CNRS UMR C5559, Observatoire de Grenoble,
Université J. Fourier, BP 53X, 38041 Grenoble Cedex 9, FRANCE
[2]Département de Géosciences, Université de Franche-Comté, 16, route de Gray, 25030 Besançon Cedex, FRANCE
[3]Institut de Physique du Globe de Paris, 4, place Jussieu, 75252 Paris Cedex 05, FRANCE
** present address: 211 Beekman St., Saratoga Springs, N.Y., 12866, U.S.A.
*** present address: Institut Français du Petrole, Rueil Malmaison, France

* corresponding author (hellmann@obs.ujf-grenoble.fr)

Abstract—To investigate pressure solution creep, chalk from the Paris basin (France) was deformed in a triaxial press with fluids. Experiments were conducted either under chemically closed (no fluid flow) or chemically open (fluid flow) conditions. In all experiments, the vertical stress (σ_1) and the lateral stress (σ_3) were independently controlled, with $4.0 < \sigma_1 \leq 8.0$ MPa and $\sigma_3 = 4.0$ MPa; the pore fluid pressure was ≤ 0.3 MPa. In each experiment, axial strain (ε) was recorded as a function of time; experiments ranged from 30 to almost 700 days.

Two experiments were examined in detail in order to study porosity reduction associated with pressure solution deformation and mass redistribution. Porosities and pore diameter distributions were measured analytically; porosities were also simulated using binarized SEM images. Porosity is reduced in the direction of fluid flow; however, the changes in porosity (up to ≈10 porosity %) are heterogeneously distributed. Computerized x-ray tomography (CT) of the same two samples reveals the presence of high-density/low-porosity regions adjacent and upstream of the interface between the two cores making up each of the samples. These low-porosity regions are interpreted to be the result of precipitation in pore spaces, but this interpretation is not certain due to the initial heterogeneous nature of the chalk. The binarized SEM images were also used to calculate the transport properties of the samples, based on the method of reconstructed porous media (Adler et al., 1990). The simulated permeabilities are the same order of magnitude as many chalk permeabilities published in the literature.

1. INTRODUCTION

Pressure solution is a commonly occurring water-rock interaction process at shallow to moderate depths. Perhaps more importantly, pressure solution (which is also referred to as intergranular pressure solution (*ips*) creep) is considered to be an important mechanism of rock deformation in the upper crust, along with mechanical compaction, cataclasis, and plastic deformation. The effective result of pressure solution is the deformation of individual mineral grains due to intergranular dissolution, and precipitation of material in pore spaces, leading to a global compaction of the rock matrix, and in general, a concomitant decrease in permeability. A general review of pressure solution can be found in Part 1.

Pressure solution creep has been extensively documented in the field. Stylolites are perhaps the most obvious feature and are especially noticeable in limestones, sandstones, and evaporites (see extensive discussions in Bathurst, 1995; Merino, 1992; for theoretical stylolite models, see Merino et al., 1983, Dewers and Ortoleva, 1990). Other pressure solution features include pressure solution cleavage (Onasch, 1983; Gratier, 1987), differentiated crenulation cleavage (Gray and Durney, 1979), and secondary mineral growth in pressure shadows and along fault planes (Bayly, 1987; Gratier, 1987; Gratier and Gamond, 1990). On a smaller scale, grain indentation (e.g., Gratier et al., 1999), fitted intergranular rock fabrics, and secondary overgrowths on grains (e.g., Dewers and Hajash, 1995) are features typically associated with pressure solution deformation. Taken together, all of these geological features document the preferential dissolution of minerals in zones of elevated stress and precipitation in zones of minimum stress. An extensive review of low-temperature deformation features (from outcrop to thin section scale) and their mechanisms of formation, including many due to pressure solution, can be found in Groshong (1988).

Pressure solution has also been shown to apply to weathering profiles and pseudomorphic replacement reactions. Based on authigenic fabrics of mineral grains, it has been suggested that when one mineral grain grows at the expense of another (i.e., dissolution via pressure solution), a kinetic-rheological feedback establishes itself such that the rate of pressure solution and the rate of crystallization eventually become equal, such that the overall volume of rock is preserved (Merino et al., 1993, 1994; Nahon and Merino, 1997; Merino and Dewers, 1998).

Numerous experimental studies of pressure solution deformation on a variety of geological materials have been carried out (see *Introduction*, Part 1), mainly with the aim of establishing constitutive relationships. In a few of these studies, detailed microscopic examinations have been carried out on the deformed aggregates. These aggregates often show grains with indentation, truncation, and overgrowth features (e.g., halite: Spiers and Brzesowsky, 1993; gypsum: de Meer and Spiers, 1995, 1997; sandstone: Dewers and Hajash, 1995). These features are interpreted to be due to pressure solution: truncation and indendation from preferential intergranular dissolution, and grain overgrowths due to precipitation in pore spaces (for details, see section 2, Part 1).

Truncation, indentation, and overgrowths are markers of mass redistribution that occur during aggregate compaction. Mass redistribution induced by pressure solution has been the subject of both theoretical and experimental studies. Modeling the evolution of curved solid-fluid phase boundaries associated with fluid-filled pores embedded in a stressed solid matrix (Reuschlé et al., 1988; Heidug and Leroy, 1994; Leroy and Heidug, 1994) is an example of a theoretical approach to understanding mass redistribution. Experimental studies have dealt with closely related subjects, such as changes in fluid inclusion geometry (Gratier and Jenatton, 1984) and crack healing (Smith and Evans, 1984; Brantley et al., 1990; Gratier et al., 1994).

An important reason for studying deformation and mass redistribution is understanding how these result in changes of pore geometry and total porosity. Pore structure and porosity are important since they affect the physical and fluid transport properties of rocks (e.g.,Walsh, 1965; Heard and Page, 1982; Evans et al., 1999). Fluid transport in rock is pertinent not only with respect to promoting chemical reactions between fluids and rock grains (e.g., pressure solution), but also because local changes in connected porosity and permeability directly affect the fluid pore pressure, and therefore the effective state of stress (Brace, 1972).

Dissolution and precipitation reactions in porous media have been addressed in many numerical modeling studies (e.g., Sallès et al., 1993; Békri et al., 1995, 1997; Mourzenko et al., 1996). Such numerical models allow for the prediction of how pore geometries and total porosity evolve under various conditions, and how this affects the fluid transport properties of the medium. Other studies have modeled porosity reduction in porous media/sediments as a function of depth, and implicitly include pressure solution creep (e.g., Lemée and Guéguen, 1996; Renard et al., 1999). Experimental pressure solution creep experiments that have measured total porosity reduction as a function of strain are quite numerous. A few of these studies have also measured reductions in aggregate porosity at the thin section scale (e.g., Dewers and Hajash, 1995). In general, however, attempts to quantify the temporal and spatial evolution of porosity during deformation are not numerous, and for this reason, detailed studies are needed.

In this study (Part 2), we examine the spatial changes in porosity in deformed chalk samples. The specific questions we were aiming to resolve concern both the degree of total porosity reduction as a function of strain and the spatial distribution of porosity reduction. This has been effected by measuring in detail the porosity changes of two experiments, L9-11 and L16, based on three commonly used porosity measurement techniques. Another important aim of this research was to apply the powerful computerized x-ray tomography technique to study post-deformation porosity and compaction, and to tie this in with the porosity data obtained by classical techniques. This technique also allowed us to make inferences concerning fluid percolation. Finally, we also applied a theoretical approach that allowed for fluid transport properties to be estimated. This approach is based on image analyses of SEM photomicrographs and the application of the "reconstructed porous media" method (Adler et al., 1990). This multi-technique approach has provided semi-quantitative information concerning the coupled processes of compaction, deformation, and mass redistribution that characterize the experimental deformation of chalk by pressure solution.

2. METHODS AND TECHNIQUES

This communication (Part 2) is based on SEM, porosity, and X-ray tomography measurements of deformed chalk, and specifically, on two experiments that used 200-mm long cores (expts. L9-11 and L16). Because the chalk is very fragile, it was not possible to core a single 200-mm long cylinder; instead, two smaller cores, approximately the same length, were placed end-to-end. The top and bottom faces of each core were cut and sanded perpendicular to the core axis. The deformation history of these two experiments is detailed in Part 1. Detailed information concerning the experimental materials and procedures is also given in Part 1.

2.1. Porosimetry

The porosity of the chalk was measured by 3 separate techniques. The connected and occluded porosity of the chalk were measured both before and after deformation using the Hg injection technique on sample volumes of ≈ 0.5-1 cm^3. The average connected and occluded porosities of undeformed chalk are 41.5 and 10.7%, respectively. Another technique (using the same Hg injection apparatus) is based on a determination of the density of samples, assuming that samples were only composed of calcite. A third technique, based on saturation of samples with water, used much larger samples, with volumes on the order of 6-8 cm^3. The porosity of a reference, undeformed sample ranged from 39.9-41.5% (based on these 3 techniques). The measurement of post-deformation porosities was effected by cutting the chalk cores in half along the core axis and extracting samples from the inside surface of each half-core.

The Hg injection technique was also used for the determination of pore space diameter distributions. The accessibility of pore spaces with a given radius (r) is a function of the Hg injection pressure (P), the surface tension of mercury (γ), and the solid-Hg interfacial angle (θ); a commonly used equation is $r = 2\gamma \cos \theta / P$ (Rootare, 1970; Gregg and Sing, 1982). In this study, the maximum Hg injection pressure was 150 MPa, which permitted Hg access to pores with $\phi \approx 0.01$ μm. After injection of Hg at high pressures, the exterior pressure relative to the sample is lowered to ambient pressure, forcing most of the Hg in the sample pore spaces to be evacuated. The fraction of Hg that remains trapped in very small pore spaces is the basis for the calculation of the occluded porosity. However, the exact physical meaning of occluded porosity measurements is not straightforward. Occluded porosity can be interpreted to be related to disconnected porosity (i.e., the porosity which is not effective in transmitting fluids), but verification of this is not possible without an appropriate and independent measurement technique. In addition, it should be noted that occluded and disconnected porosity measurements depend on the physical characteristics (e.g., viscosity, surface tension) of the injected fluid; thus, results based on Hg measurements may differ quantitatively from those based on aqueous fluids, for instance.

2.2. SEM Image Analysis

SEM photomicrographs from an undeformed reference sample, as well as from post-deformation samples, were used to investigate compaction; these are discussed further on in the *Results and Discussion* section. A large series of SEM images realized of experiments L16 and L9-11 (post deformation) were also analyzed for the derivation of simulated porosities and permeabilities. This series of images was based on a sampling technique that minimizes the danger of mechanically disturbing the matrix. Each plug that was extracted from a sample was cut into two parts, one for SEM images, the other for porosity measurements. Each SEM plug was impregnated with a low-viscosity resin that imparted enough rigidity to the matrix so that it could be dimensioned for SEM use. A second impregnation step filled all remaining pores. In both impregnation steps, only capillary forces were responsible for the penetration of pore spaces (i.e., no vacuum techniques were used, this ensured that the matrix remained undisturbed). The impregnation steps were followed by gentle polishing of the surfaces that were viewed by SEM. The color difference between the resin and the solid matrix was sufficient for the discrimination of pore spaces and grains.

Four corner areas on each sample plug were chosen for SEM imaging. Using the code Visilog, each SEM image was binarized, with white representing pore spaces and black representing matrix material. The process of binarization was interactive (i.e., gray-scale threshold, erosion and dilatation cycles) to ensure that the binarized image resembled as much as possible the spatial porosity characteristics of the original SEM image (i.e., by visual comparison, comparison of measured and 2-D binarized porosity). Even though this step introduces a certain subjectivity to the procedure, experience has shown this to be the most precise manner for faithfully reproducing the real pore space structure (Adler, 1994; see also discussion in Gaviglio et al., 1997 on the effects of interactive processing).

SEM images were taken at 50x and 2000x magnification. Porosities based on the 50x images are termed "mesoporosity", while those based on the 2000x images are termed "microporosity". The mesoporosity is on the order of ≤ 1%, while the microporosity is ≈ 34%. This extreme difference in values shows the importance of the pixel to pore size ratio in determining porosities. It should be noted, however, that porosity and magnification are not correlated beyond a certain level of image magnification (as shown in Section *3.3*). Since the microporosity values were closest to the measured values of bulk porosity, only microporosities were considered to be useful for this study.

2.3. Simulated Porosity and Permeability Calculations

Each binary image was analyzed using the "reconstructed porous media" method developed by Adler and coworkers (Adler et al., 1990, 1992; Adler, 1994; for the development of this technique, see Joshi, 1974; Quiblier, 1984); a brief overview of this method follows. For any point x within a binary image, a phase function $Z(x)$ can be used to differentiate between solids and pore spaces:

$$Z(x) = 1 \quad x \in \text{pore space}$$
$$0 \quad x \in \text{solid phase} \tag{1a}$$

The porosity can then be defined as

$$\phi = \overline{Z(x)} \tag{1b}$$

where the overbar denotes a statistical average. Another important quantity is the correlation function $R_z(u)$, which is defined by the second moment of the phase function:

$$R_z(u) = \overline{[Z(x) - \phi] \cdot [Z(x+u) - \phi]} \,/\, (\phi - \phi^2) \tag{2}$$

where u is the displacement vector. The correlation function quantifies the statistical organization of the porous medium; it also can be defined by the probability that two points belong to the same phase.

The subsequent generation of a three-dimensional medium with porosity ϕ and correlation function $R_z(u)$ is based on the generation of a random function of space $Z(x)$, where $Z(x) = 0$ in a solid phase and $Z(x) = 1$ in a liquid phase. In addition, $Z(x)$ must satisfy the conditions given by Eqns. 1b and 2. The resulting reconstructed porous medium is portrayed in terms of small cubes that are either liquid or solid-filled. Transport behavior associated with reconstructed media can be calculated from the usual Stokes equations; this permits the determination of the flow field (assuming Newtonian fluids at low Reynold's numbers). Once the flow field is determined, the calculation of various transport properties follows (e.g., permeability, conductivity, etc.; for details on this method, see Adler et al., 1990).

2.4. X-Ray Computerized Tomography

In order to investigate the 3-D spatial density of the chalk samples, x-ray computerized tomography (CT) images were obtained of an undeformed chalk sample, as well as samples L16 and L9-11 after deformation. The imaging was carried out on a 3rd generation medical x-ray tomography unit located in a hospital (Siemens Somatom Plus S, Radiologie GHB K.U. Leuven, Belgium; instrument settings: 137 kV, 75 mA for L9-11 and non-deformed reference chalk; 120 kV, 240 mA for L16). The X-ray CT method is based on the attenuation of x-rays by the sample and the subsequent reconstruction of a section through the sample, which is portrayed in terms of the spatial variation of the radiological density (see e.g., Hounsfield, 1973; Herman, 1980; Wellington and Vinegar, 1987; and references therein; for recent geological applications, see e.g., Raynaud et al., 1989; Verhelst et al., 1995; Géraud et al., 1998; Brown et al., 1999). For monochromatic x-rays, the linear attenuation coefficient is a material constant, such that x-ray density variations are due to differences in the bulk density. The main advantage of this method, which is completely non-destructive, is that it can provide a series of sequential density images (i.e., density slices) of a sample.

The radiological density variations of the bulk chalk matrix can be directly related to porosity variations, based on the fact that the matrix is composed exclusively of calcite (as confirmed by x-ray diffraction and SEM/EDX results; with the exception of chert fragments). The application of this technique in the present study is qualitative, however, for the following reasons: first, the CT scanner reconstruction algorithms (ultra-high resolution AH_07541) were fixed for applications related to medical reconstructions of the human head; no modifications were attempted for this study; and second, a quantitative approach requires the calibration of the gray-scale densities to an exact porosity scale. Nevertheless, this technique proved to be very powerful in that it yielded important qualitative information on the initial heterogeneous structures of the chalk, as well as the changes in porosity that resulted from the combined effects of pressure solution deformation, fluid percolation, and mass redistribution by precipitation in pore spaces.

3. RESULTS AND DISCUSSION

3.1. SEM Images

SEM images were taken with several objectives in mind: (a) recognition of matrix compaction and porosity reduction, (b) identification of possible fluid pathways, and (c) the numerical 3-D reconstruction of porous media after deformation, based on binarized SEM images (discussed further on). The interpretation of SEM images, based on both undeformed and deformed samples, proved to be difficult with respect to identifying fluid flow pathways and the effects of compaction, as discussed below.

Both undeformed and deformed chalk samples show the presence of pore spaces, with typical diameters ranging from one to several μm, as seen in Fig. 1a. Figure 1b shows a thin vein that cross-cuts an undeformed chalk matrix. These veins are composed of the same material as the chalk matrix (as confirmed by SEM/EDX analyses), but have more calcite cement, and are more compact and less porous than the matrix.

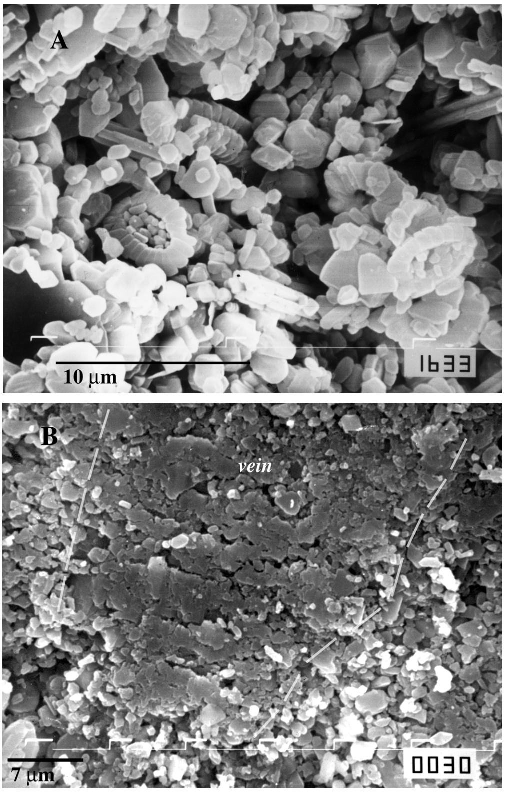

Fig. 1. SEM images of Guerville chalk used in study. (a) The chalk is composed primarily of coccolith skeletal debris and other shell fragments; note the high porosity inherent to this chalk (≈ 40%). (b) Vein crosscutting the matrix; the porosity is considerably diminished in comparison to surrounding matrix.

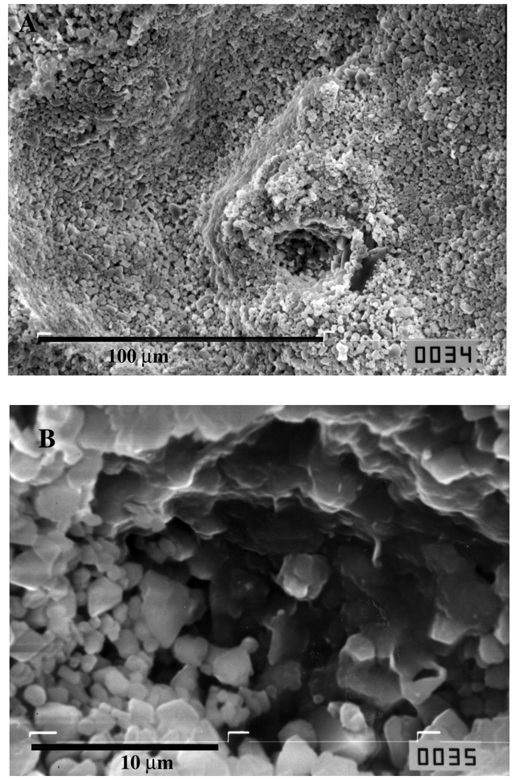

Fig. 2. (a) An example of a large channel present in deformed chalk (expt. S8-9); (b) an enlarged view. Large channels such as these are present both in undeformed and deformed samples. Their axial continuity is not known, but they may play a significant role in preferential fluid flow.

Occurring less frequently are large channel-like structures with diameters often exceeding 10 µm; one such channel is shown in Fig. 2. These structures were observed by SEM both in undeformed and deformed chalk samples. The origin of such large channels is not known; they may represent a primary feature, having formed during sedimentation and/or diagenesis; alternatively, they may be secondary dissolution features, having formed in situ due to groundwater percolation, for example. These channels apparently were not destroyed during deformation in the laboratory. In fact, it is possible that they may have been enlarged by fluid circulation during the experiments, this having occurred concomitantly with compaction, reduction in pore space volumes, and decreasing permeability of the matrix. The exact relationship between these channels, pressure solution, and fluid flow during experimental deformation remains an open question, however.

According to studies by Gaviglio et al. (1993, 1997) on the Mons basin chalks, large channels (ϕ = 1- 10 µm, and in some cases $\phi > 10$ µm) most commonly occur immediately adjacent to fault planes; these authors postulate that channels form (or are enlarged) as a consequence of the initial stages of deformation in the presence of fluids, and are kept open by fluid circulation even during compaction of the surrounding matrix. Their observations imply that large channels characteristically form in chalks that have undergone deformation in the presence of fluids. Nonetheless, the two dimensional nature of SEM images in this study makes the interpretation of these channels and pore spaces tenuous, especially since it is not possible to ascertain their connectivity. For this reason, it is difficult to determine the exact pathways and fluxes associated with fluids percolating through the samples during experimental deformation runs.

It is interesting to note that SEM images of the interface between the two cores comprising sample L9-

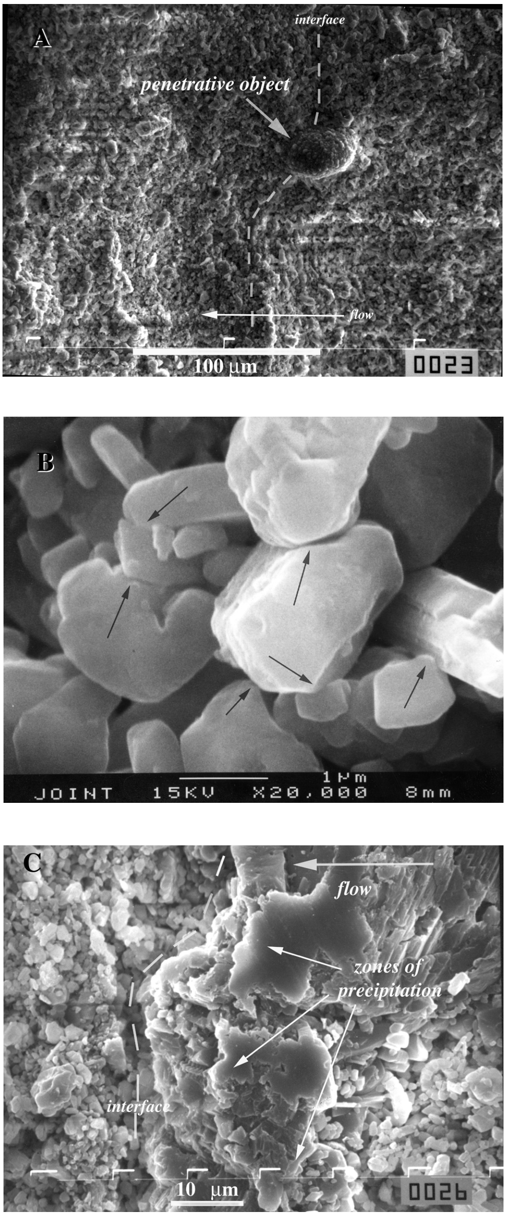

Fig. 3. (a) SEM image of the irregular interface (dashed line) between the 2 cores of L9-11; the irregular nature suggests stylolite formation. The large object that straddles the interface has acted as a resistant indenter and has penetrated both cores (i.e., by pressure solution). (b) Examples from L9-11 of grain-to-grain indentation and truncation due to pressure solution, as indicated by arrows. (c) SEM image of interface between the two cores in L9-11 (dashed line). The upstream core, shown on the right, shows the presence of large, cemented areas; these are interpreted to be due to precipitation as a consequence of pressure solution deformation and mass redistribution.

11 reveal it to be highly irregular (see Figs. 3a, c) after deformation, perhaps indicating the onset of stylolite formation. The irregularity is most probably due to a combination of mechanical and chemical processes (i.e., pressure solution reactions) acting upon the interfacial boundary. Figure 3a shows the presence of a large, resistant object situated at the interface that has acted as an indenter with respect to both cores during the experimental deformation. The penetration of this object into both cores can be explained in terms pressure solution leading to preferential dissolution of the matrices perpendicular to the direction of major stress (this can be compared to laboratory and natural examples - e.g., Gratier et al., 1999). Evidence for pressure solution at the scale of individual grains, as evidenced by grain indentation and truncation, is shown in Fig. 3b. It should be noted, however, that even though this image was taken of grains from the interfacial region of L9-11 after deformation, there is no proof that these pressure solution features do not owe their origin to the some kind of paleo-pressure solution deformation (i.e., pressure solution features possibly present in original samples).

Perhaps the most predictable consequence of deformation associated with fluid flow and pressure solution is compaction of the granular chalk matrix. However, a comparison of SEM images of undeformed and deformed chalk samples does not reveal any discernable differences in the degree of matrix compaction. A qualitative comparison of the undeformed chalk matrix in Fig. 1 with the deformed chalk matrix of L9-11 (Fig. 3) underscores this point. This is most probably due to the very modest degree of compaction experienced by the sample (1.5% strain, see Fig. 5b, Part 1).

Figure 3c also clearly shows the exact nature of the interface between the two cores of L9-11. The void space that defines the interface in the image has a thickness < 1 µm, which is roughly the same dimension as many of the pore spaces found throughout the matrix. The chalk matrices on both sides of the interface do not reveal any obvious, qualitative differences in compaction or porosity. Nonetheless, a few of the areas adjacent to the upstream side of the interface do show grain "welding" and coalescence due to cement overgrowths (see Fig. 3c). These low-porosity regions, which always end abruptly at the interface, resemble very closely the veins shown in Fig. 1b. In addition, the cemented grains shown in Fig. 3c resemble very closely coalesced grains found in chalks that have been deformed and compacted adjacent to fault planes (Fig. 4, Gaviglio et al., 1993). This close resemblance suggests a transformation of the matrix, due most probably to precipitation of calcium carbonate in pore spaces. The interfacial region of L9-11 proved to be of

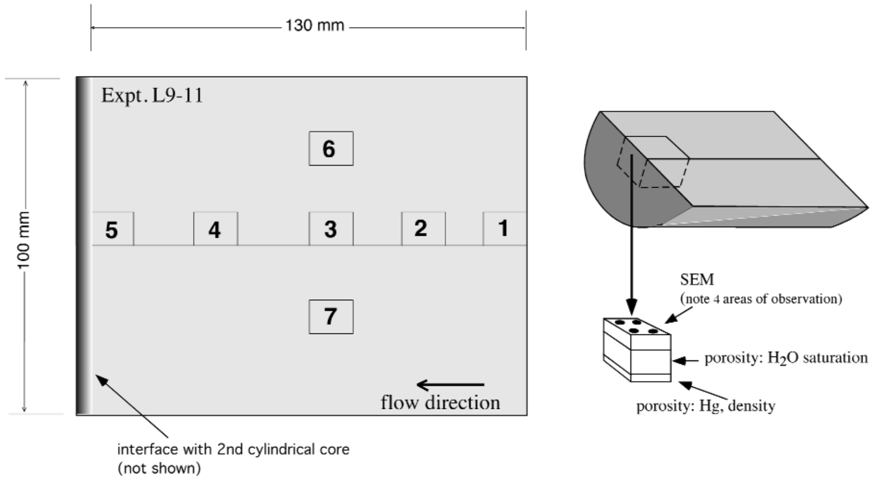

Fig. 4. The figure on the right shows how all cores were cut along the axis and sampled after deformation, as well as the partitioning of samples for SEM imaging and porosity measurements. The left-hand figure shows the sample localities within the upstream core of L9-11.

special interest since this same area corresponds to a large contrast in x-ray tomographic density (see Fig. 16). As discussed further on, this density contrast corresponds to a difference in matrix porosities on adjacent, but opposite sides of the interface.

3.2. Porosimetry

3.2.1. Reference and experiment L9-11 porosities

The average porosities of undeformed chalk samples, based on the Hg injection, density, and water saturation methods, are 41.5, 41.3% (avg. of 3 samples, $1\sigma = 2.1$ porosity %), and 39.9% (avg. of 7 samples, $1\sigma = 0.9$ porosity %), respectively. Multiple Hg injection measurements were not performed on a reference sample, but the accuracy and precision of this technique is roughly the same as the density method, based on measurements of other chalks. In the description of porosities below, simulated porosities, based on binarized images and the method of reconstructed porous media, are also presented for comparison with measured values (see section *3.3* for more details). The average simulated porosity of an undeformed chalk sample is 33.6% (avg. from 4 separate images, $1\sigma = 4.5$ porosity %); note that this is considerably lower than the average of the measured values. The uncertainties of porosities associated with deformed samples (measured and simulated) are given directly in the pertinent figures.

Figure 4 shows schematically the manner in which extracted plugs were divided up for SEM and porosity measurements. In addition, the locations of the plugs, the direction of fluid flow, and the interface between the 2 cores for experiment L9-11 are shown.

Figure 5 represents the cumulative distribution curves of the pore diameters (Hg-injection method) associated with the 7 locations given in Fig. 4, as well as for a non-deformed sample (reference). Even though there is some variation in the pore distribution curves of samples 1, 2, 3, 6, and 7 with respect to the reference, they are statistically equivalent, based on the analytical uncertainties. On the other hand, samples 4 and 5 show diminished porosities and a noticeable and significant shift in their pore distributions towards smaller diameters (i.e., increase in pore space population: $0.1 < \phi < 1$ μm).

Figure 6a shows the evolution of the porosities as a function of axial distance and flow direction (i.e., samples 1-5 in Fig. 4). The porosities are based on Hg-injection and density measurements, as well as simulated values. The simulated porosities have uncertainties ranging from 0.9 to 6.1 porosity %, with an average uncertainty of 3.6 porosity % (based on sample nos. 1-7, 1σ uncertainties). For any given sample location, the maximum difference between the various porosities (analytical vs. simulated) varies from 2 to 8 porosity %. However, the trends of all of the profiles reveal a decrease of roughly 5 porosity % between the upstream and downstream ends of the core. The occluded porosity, also shown in Fig. 6a, reveals a modest increase along the core axis and direction of flow, which is in accord with the shift towards smaller

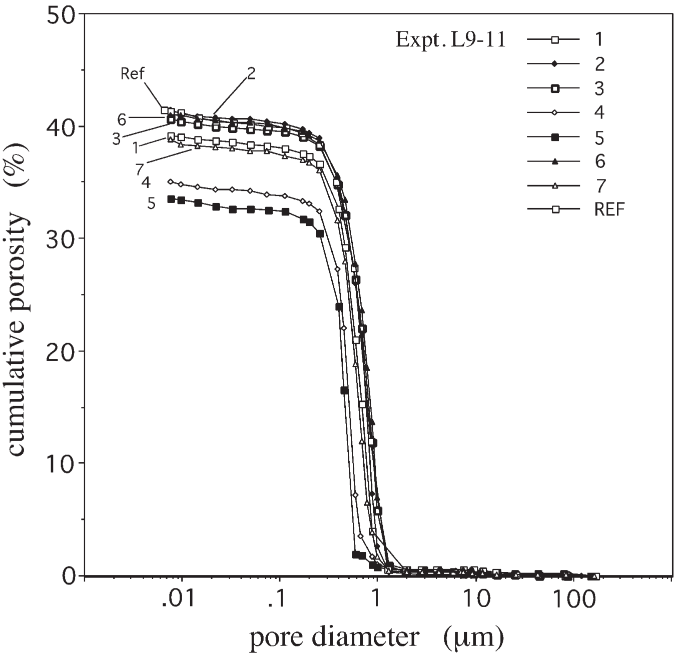

Fig. 5. Cumulative pore diameter distribution curves for samples 1-7 of L9-11 and an undeformed reference. Samples 4 and 5 show diminished porosities and a shift in pore distributions towards smaller pore diameters ($0.1 < \phi < 1$ µm).

pore diameters shown by the pore distribution curves in Fig. 5 (i.e., distributions 1, 2, 3, ref. vs. 4, 5). A graph of the ratio of occluded porosity to total porosity as a function of axial position (Fig. 6b) shows more concisely the significant diminution of the total connected pore space volume towards the downstream end of the sample L9-11, close to the interface with the other core (see Fig. 4).

3.2.2. Experiment L16 porosities

The porosities of L16 were more extensively sampled and measured in comparison to expt. L9-11. Figure 7 portrays the 55 sampling locations where the porosities where measured by the water saturation method; in addition, the porosities at 8 of these locations were also measured by the Hg injection and density methods, and simulated by the reconstructed porous media method. Also shown is the location of the interface between the two cores of expt. L16, which are designated as the 'upstream' and 'downstream' cores. The 8 simulated porosities have uncertainties (1σ) ranging from 2.1 to 8.7 porosity %, with an average of 4.9 porosity % (based on sample nos. 3, 18, 28, 33, 43, 53).

The pore distribution curves associated with the aforementioned 8 localities, shown in Fig. 8a, show a general shift towards reduced porosities and smaller pore diameters with respect to the reference. The most pronounced differences were measured for the samples adjacent to the interface between the two cores (nos. 33 and 35-see Fig. 7). The reduced porosity and the shift towards smaller pore diameters associated with sample 33 vs. a reference sample is indicated more clearly in Fig. 8b. This example shows that the median pore size diameter decreases from 0.8 to 0.3 µm. The pore diameter shifts (with respect to the reference) of all of the distribution curves in Fig. 8a do not follow any obvious generalized trend, as evidenced, for example, by a strong shift associated with sample no. 3 (located at the inflow end of the upstream core) and no shift for no. 28 (adjacent to the upstream side of the interface).

The 55 water saturation-based porosities are shown graphically in Fig. 9 in terms of a gray scale, with black representing the maximum porosity (40.4%) and white the minimum porosity (29.5%) measured. The highest variation in porosities occurs in the upstream core, whereas the downstream core generally shows a higher total porosity. The overall gray scale pattern does not indicate any obvious zones of connected high porosity which might be associated with preferential fluid flow (i.e., on a cm-scale). Nonetheless, two patterns stand out: a. the left-hand side of both cores shows a continu-

A.

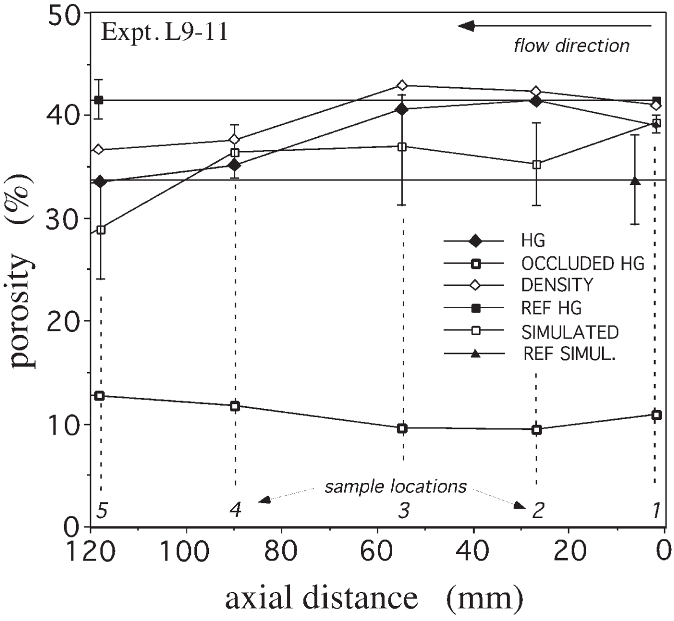

B.

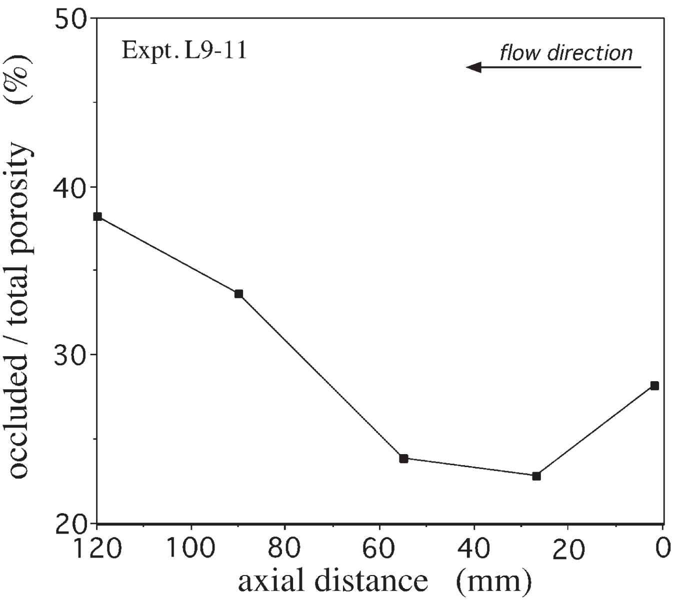

Fig. 6. (a) Axial porosity trends for L9-11, based on samples 1-5. Porosity measurements are based on Hg injection, density, and water saturation methods; in addition, simulated porosities are shown for comparison. All of the trends show a general decrease in porosity towards the downstream direction, with the exception of the occluded porosity, which increases in the direction of flow. Error bars represent $\pm 1\sigma$. (b) The marked increase in the ratio of occluded to total porosity towards the downstream end of the core reveals the combined effect of decreasing porosity and increasing unconnected pore space volume.

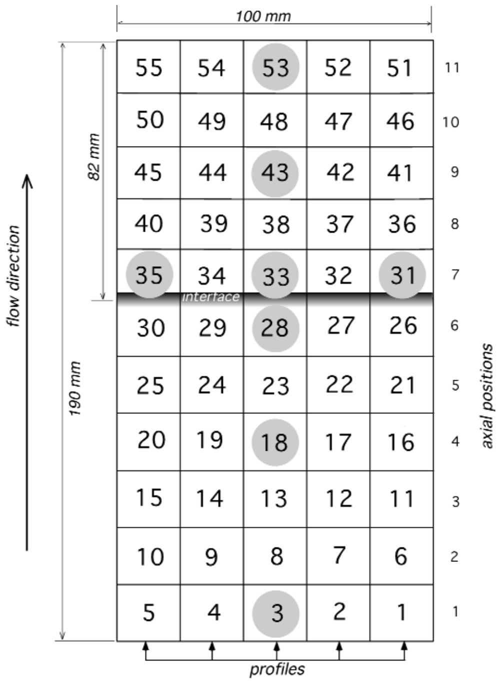

Expt. L16

Fig. 7. Expt. L16 sample locations (cut-away view along axis - as in Fig. 4): porosities 1-55 were measured by the water saturation method, whereas samples 3, 18, 28, 31, 33, 35, 43, and 53 were also measured by the Hg injection and density methods; the porosities of these samples were also simulated. The indicated axial positions and profiles refer to Figs. 10 and 11a.

ous zone of intermediate to low porosity b. the upstream core immediately adjacent to the interface between the two cores is marked by a continuous band of very low porosity, ranging from 30.1 to 31.1%.

Five longitudinal profiles corresponding to the gray-scale porosities in Fig. 9 are shown in Fig. 10. The upstream profiles show a general decrease in porosities in the direction of flow, up to the interface, followed by a sudden increase on the downstream side of the interface. Figure 11a also portrays longitudinal profiles, based on measured and simulated porosities corresponding to the central axis (profile 3, Fig. 7). As opposed to the measured and simulated porosities of L9-11 shown in Fig. 6a, the correlation between the measured and simulated porosities is poor, and in addition, the measured porosities do not agree with each other (i.e., water saturation vs. Hg injection and density measurements). Nevertheless, the Hg injection and density porosity profiles do show a marked minimum adjacent to the interface, but on the downstream side (as opposed to the upstream side, as with the water saturation results). The poor correlation of the measured porosities may be due to real differences (i.e., due to the different volumes analyzed - see Fig. 4). On the other hand, there may have been a slight inaccuracy in the exact location of sampling for each method with respect to the interface, such that the minima in porosities actually correspond to the same location (i.e., upstream and immediately adjacent to the interface); if this is the case, then the trends of the measured porosities are in better accord.

Figure 11a shows that the simulated porosities range from ≈ 20-50% over the entire length of sample L16; this variation is significantly higher than the variations in the measured porosities. It is interesting to note that for sample L9-11, the variations in the measured and simulated porosities over the entire length of the upstream core are approximately equivalent (Fig. 6a). This difference between the two experiments may reflect a greater amount of heterogeneous porosity reduction in L16 vs. L9-11.

The large variation in simulated porosities that was determined over the entire length of sample L16 also occurs at a single sampling locality. Figure 11b represents simulated porosities of sample 53, based on a tightly-spaced (0.33 mm-step size) lateral SEM traverse (11 mm total distance, traverse from left to right, refer to Fig. 7). Figure 11b shows that the porosity varies from ≈ 30-57%, which represents a variation similar to that determined over the entire length of L16 (i.e., simulated porosity profile in Fig. 11a). There is, however, an important difference between the simulated porosities calculated in Figs. 11a and b; they are based on SEM images with significantly different magnifications. In Fig. 11a, sample 53 has a simulated porosity of ≈ 19 % (based on 2000x images), whereas in Fig. 11b the average porosity of sample 53 is ≈ 40-45 % (based on 250x images). This example shows that the SEM image scale has a significant effect on the simulated porosities (this is discussed in more detail in the next section).

3.2.3. Comparison of techniques

Based on the results discussed above for expts. L9-11 and L16, the various analytical methods used in this study are not all equally suitable for porosity measurements of deformed porous materials, such as chalk. The Hg injection technique is invaluable due to its ability to measure the distribution of pore sizes in a sample. An additional positive point is that is possible to analyze relatively small samples using this technique (this applies to the density method, as well). On the other hand, the greater sampling volume associ-

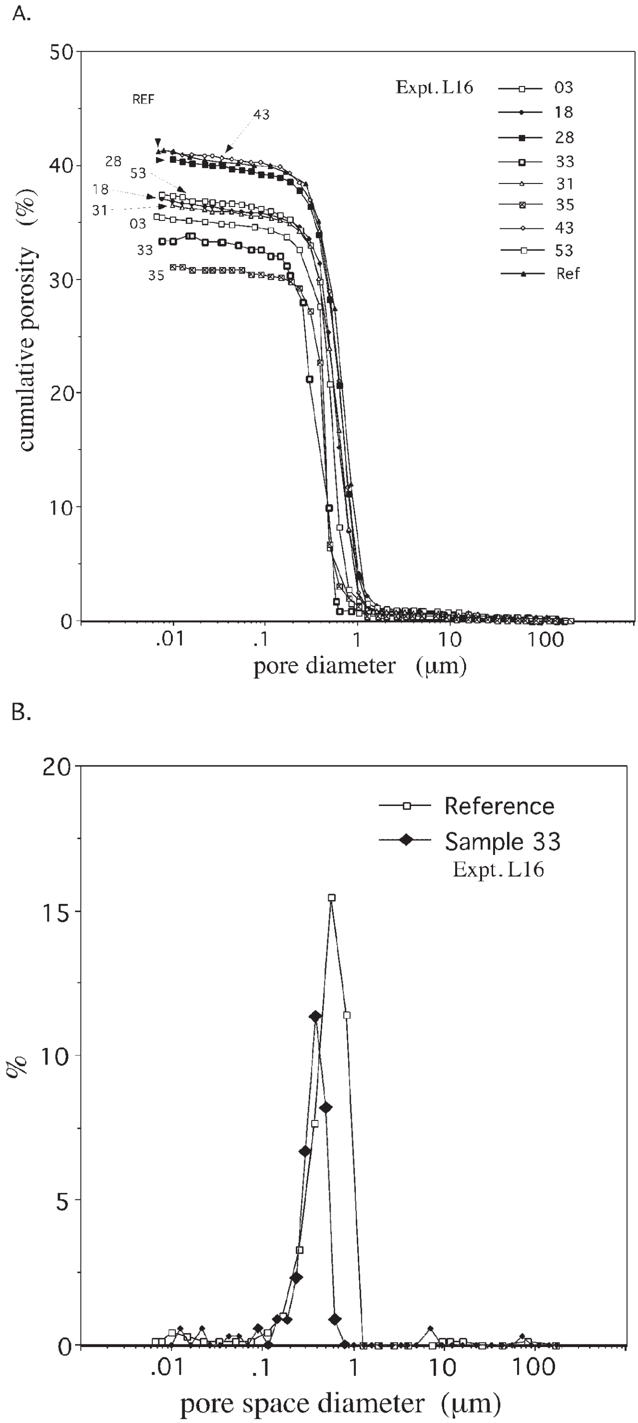

Fig. 8. (a) Cumulative pore diameter distribution curves measured by Hg injection for samples from L16 and an undeformed reference sample. The two samples adjacent to the interface (samples 33, 35) show the largest decrease in porosity and the most significant pore diameter shifts with respect to the reference. (b) Individual normalized porosity % vs. pore space diameters for sample 33 and a reference. These curves show more clearly the overall decrease in porosity of sample 33, as well as a shift in the pore diameter populations, from a median of 0.8 µm for the reference to 0.3 µm for sample 33.

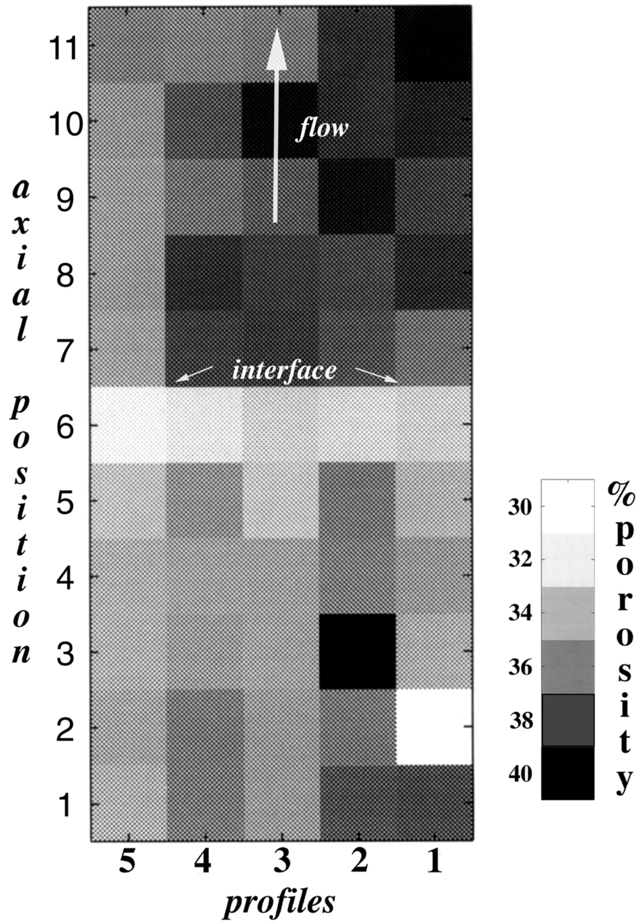

Fig. 9. Gray scale representation of water saturation porosities measured for samples 1-55, L16 (cutaway view along axis- compare to Fig. 7). The maximum measured porosity (40.4%) is indicated in black, the lowest (29.5%) is indicated in white. The overall pattern does not indicate any obvious zones of connected high porosity at the cm-scale. The most obvious feature is a zone of very low porosity (ranging from 30.1-31.1%) immediately adjacent to the interface of the two cores, on the upstream side. The indicated profiles and axial positions refer to Figs. 10 and 11a.

ated with the water saturation method presents an advantage in terms of a reduced sensitivity to local porosity heterogeneities. This translates to measurements that are more representative for heterogeneous materials. The poor accord in the measured porosity results for expt. L16 (i.e., Fig. 11a) potentially reflects an elevated ratio of local heterogeneities to volume analyzed by each technique. It is not certain why the measured porosities for L9-11 are in much better accord than those for L16, but the greater degree of deformation of L16 may have played a role in accentuating the heterogeneities already present in the chalk (L9-11: 0.015 strain vs. L16: 0.028 strain).

As shown in Figs. 6a and 11a, the accord between the measured and the simulated porosities differs with respect to expts. L9-11 and L16; in the former the accord is relatively good, whereas in the latter, the accord is poor. Local porosity heterogeneities and the scale of measurement exert a large influence on simulated porosities (e.g., Fig. 13a), probably even more so than with analytical porosity measurements. Since the simulated porosities are based on binarized SEM images, the process of binarization is the limiting factor with respect to the accuracy and the representative nature of the simulated porosities. The scale of the binarized images is critical since it influences the over-

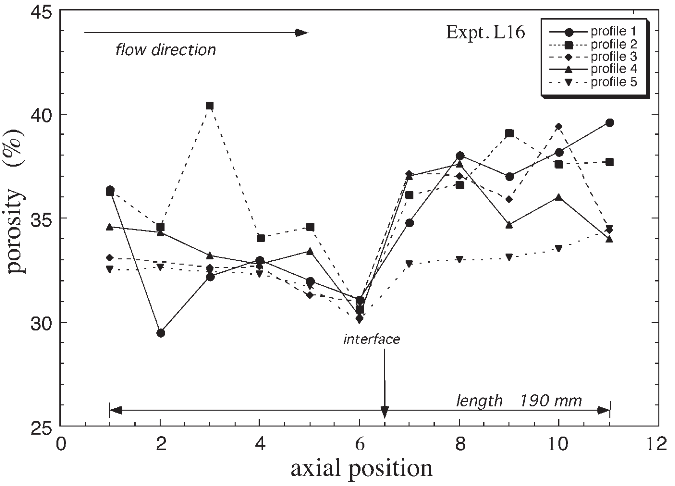

Fig. 10. Longitudinal profiles of water saturation porosities for expt. L16, as shown graphically in Fig. 9. The profiles show the heterogeneous nature of the porosities, a general decreasing porosity trend with flow direction in the upstream core, and a local porosity minima adjacent to the interface.

all values of porosity (i.e., in the extreme case, micro vs. mesoporosities, see Fig. 12), as well as their sensitivity to local heterogeneities. A comparison of the simulated porosities for sample 53 (expt. L16) shows quite well the trade-offs associated with the different scales of the binarized images. Thus, increasing the magnification of SEM images increases the resolution of the binarized images, which is crucial for accurately reproducing the subtleties of the microporous matrix structure. However, the higher the magnification, the greater the sensitivity of the simulated porosities to local heterogeneities (e.g., Fig. 13a), which in turn renders them less representative for the whole of the sample. Conversely, binarized images that are based on low magnifications cannot systematically resolve the pore spaces, resulting in simulated porosities that are perhaps less sensitive to heterogeneities, but are nonetheless, too low compared to those measured analytically.

The complex nature of deformed and heterogeneous porous materials, such as the chalk in the present study, are perhaps too complex for accurate, and at the same time, representative binarization. This is not a problem with more simple materials, such as well-sorted sandstones, where simulated porosities are very close to those measured analytically (e.g., Fontainebleau sandstone, Adler et al., 1990). Perhaps the only viable solution to increasing the accuracy of simulated porosities and transport properties of complex and heterogeneous materials is significantly increasing the number of binarized images per sample.

3.2.4. Comparison with porosities in naturally-deformed chalks

It is worthwhile at this point to compare the porosity results in this study with those from naturally deformed chalks. Extensive work in the Mons basin, Belgium (geographically close to Guerville chalk quarry-the provenance of chalk in Parts 1, 2) by Gaviglio and coworkers (Gaviglio et al., 1993, 1997), for example, has documented the physical and chemical changes induced in chalks that have undergone modest deformation due to tectonic movements along faults. A study of chalk within a graben structure (Gaviglio et al., 1993) shows that with increasing proximity to a normal fault (over a lateral distance of ≈ 4 m), chalk porosities systematically decrease by approximately 5-10 porosity %. In addition, chalk samples immediately adjacent to the fault display a much higher degree of variation in porosities as compared to non-deformed chalk, ranging from 30.3 to 37 porosity %. The effect of deformation on porosities was not found to be homogeneous, however, since weakly deformed chalks actually show slightly higher porosities (on the order of 0.7-5.5 porosity %), due apparently to grain dilatancy. Pore distribution curves (see Fig. 6, Gaviglio et al., 1993) also reflect the heterogeneous nature of deformation. Weakly deformed chalks show a modest increase in pore diameters (ϕ 1-10 μm) with respect to non-deformed chalk; strongly deformed samples (adjacent to fault) show that a large percentage of large pores (ϕ 1-10 μm) remain, even

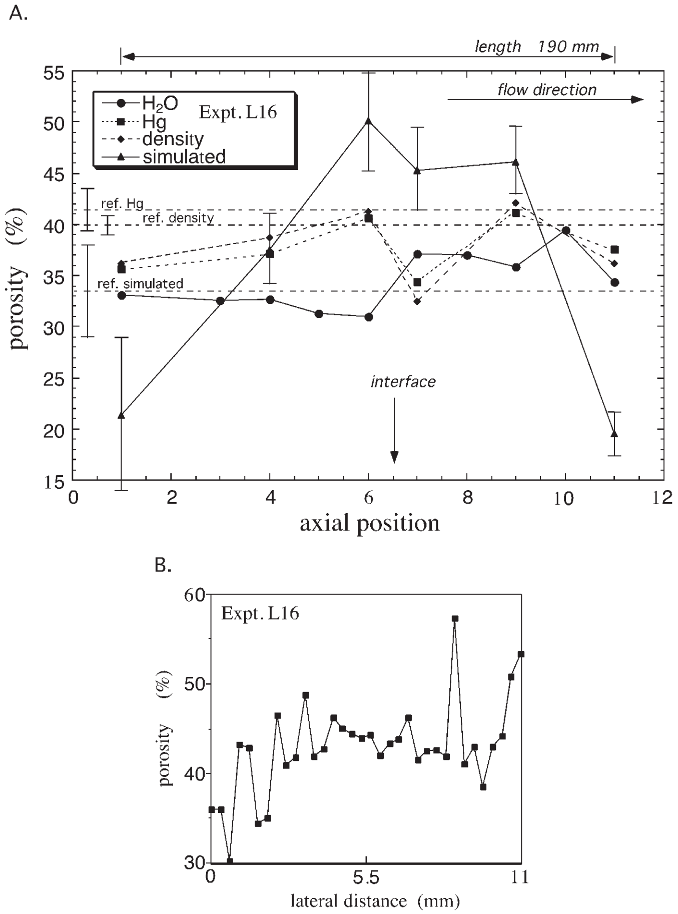

Fig. 11. (a) Comparison of various porosity profiles along the central axis of L16, based on analytical and simulated data. There is a strong discordance between the simulated data and analytical measurements; this is most probably a function of the high sensitivity of the simulated porosity determinations to local porosity heterogeneities. Error bars represent $\pm 1\sigma$. (b) Lateral simulated porosities for sample 53, L16 (refer to Fig. 7). The scattered nature of the data shows the elevated sensitivity of simulated porosities to local heterogeneities. Note that the average porosity ($\approx$43%) is much higher than for sample 53 in (a) (data point lower right corner); this is a function of different SEM magnifications- see text for details.

though the median pore distribution is shifted to smaller pore diameters (in the range of ϕ 1- 0.1 μm) with respect to non-deformed chalk (see also Fig. 10, Gaviglio et al., 1997). Gaviglio et al. (1993) attribute the overall porosity changes being due to initial dilatation of grains and enlargement of flow channels, followed by progressive porosity reduction due to pressure solution compaction and cementation. These results are complementary to those of the present study in that they show that the effects of deformation and pressure solution on chalk in both laboratory studies and natural environments can be quite heterogeneous.

3.3. Simulated Porosities and Reconstructed Porous Media

Two representative SEM images of sample 4 (expt. L9-11, see Fig. 4) are shown in Figs. 12a, b. These images represent the same area at two different magnifications, 50x and 2000x, respectively. The respective binarized images show the dramatic difference in porosities associated with these different image scales. The porosity associated with the 50x binarized image is 1%; this "mesoporosity" essentially represents large void spaces due to macroscopic fossils (e.g., upper right hand corner, Fig.

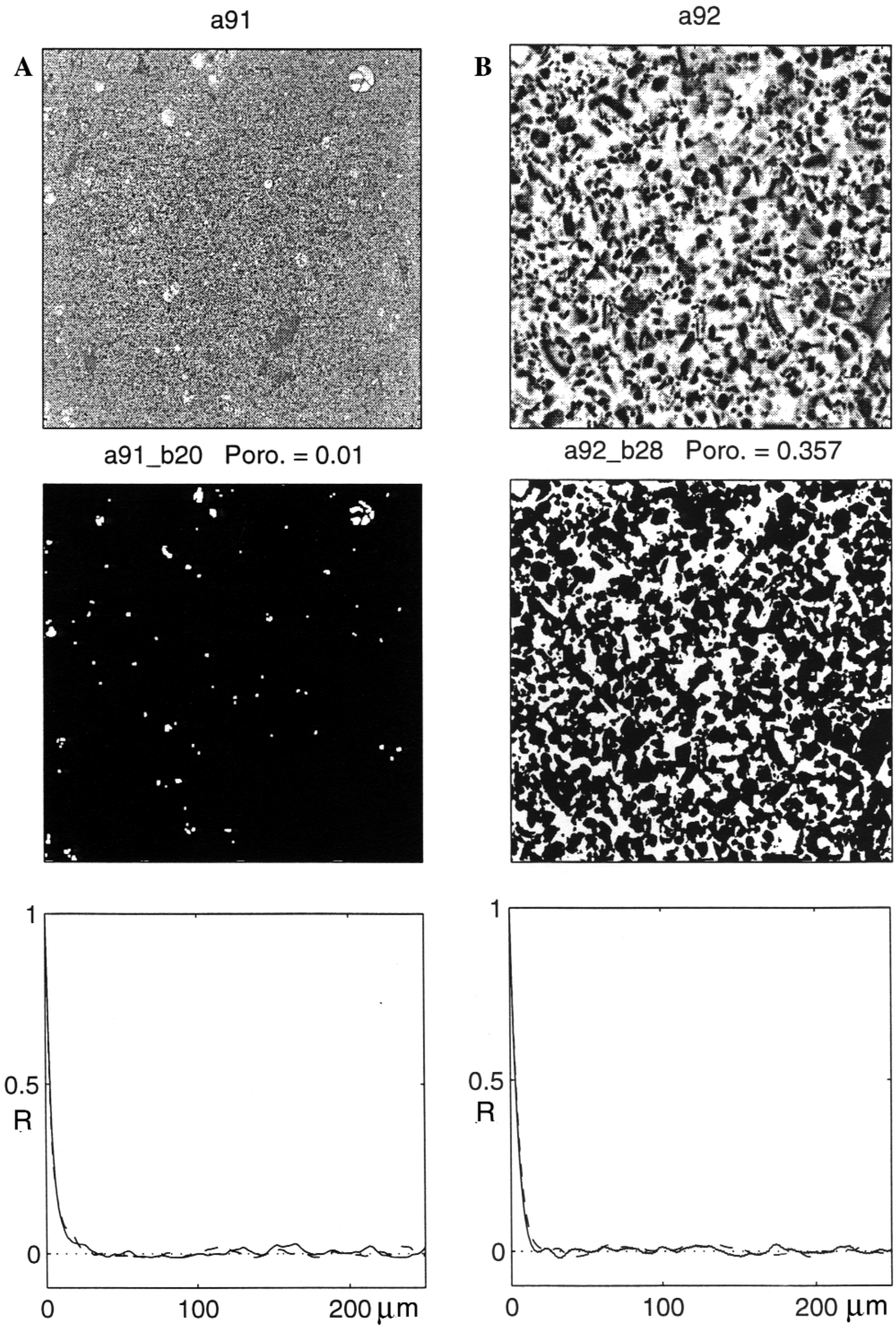

Fig. 12. SEM images (top), binarized equivalents (middle), and autocorrelation functions (bottom), based on one corner area, sample 4, L9-11. Pore spaces indicated in white, solid matrix in black. (a) Image areas 1600 x 1600 μm, top and middle. The simulated "mesoporosity" is 1%, this representing only large fossil voids (e.g., upper right hand corner) (b) Image areas 40 x 40 μm, top and middle. The simulated "microporosity" is 35.7%, in close agreement with analytical values. In both (a) and (b), the autocorrelation functions R_x (—) and R_y (---) are similar, indicating insignificant pore space anisotropy.

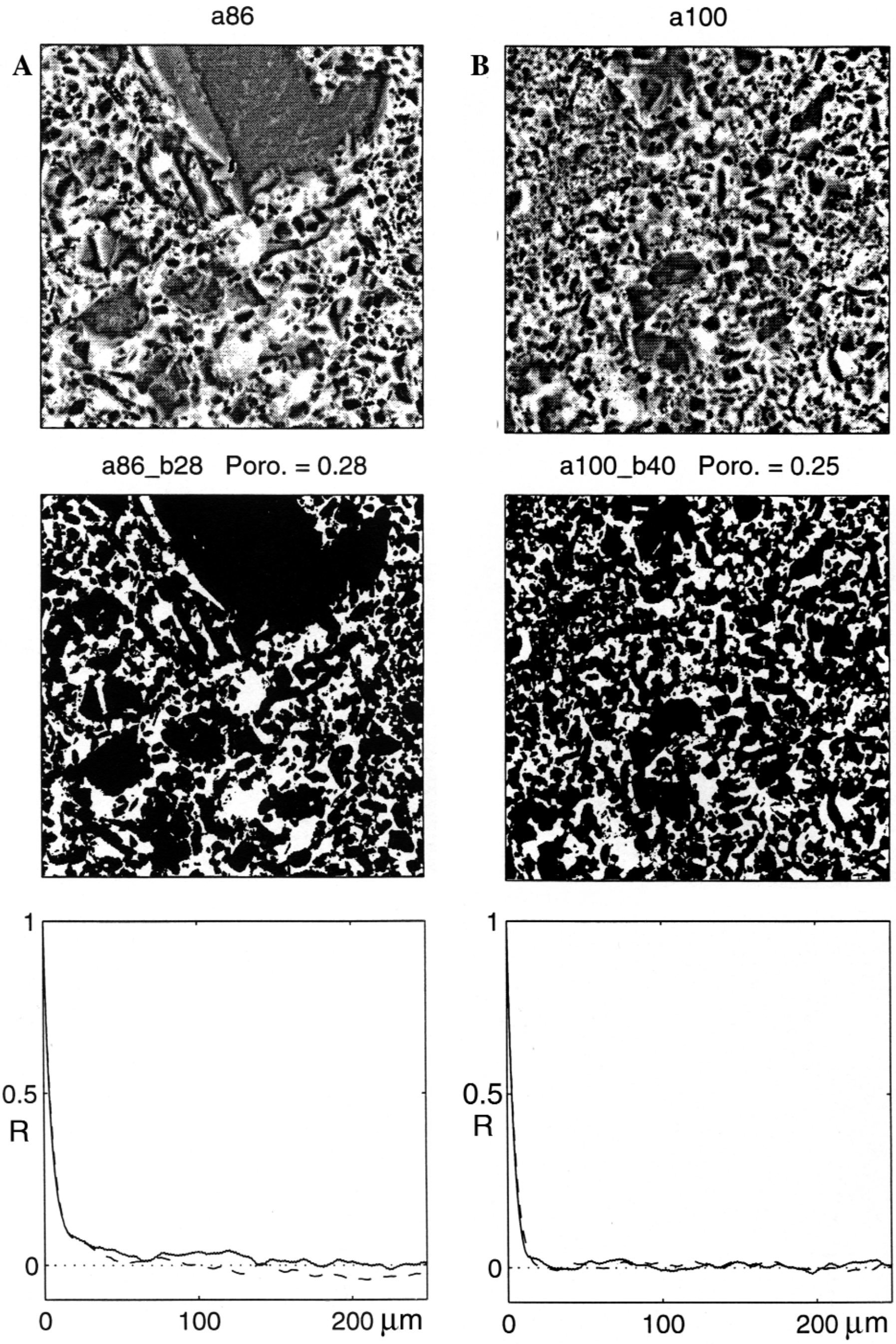

Fig. 13. SEM images (top), binarized equivalents (middle), and autocorrelation functions (bottom), based on one corner area, samples 3 and 6 in L9-11, (a) and (b) respectively. Pore spaces indicated in white, solid matrix in black. Image areas top and middle: 40 x 40 µm. (a) This image shows the sensitivity of simulated porosities to heterogeneities; in this case the simulated porosity is reduced to 28% by the large object visible in the image. The autocorrelation functions R_x (—) and R_y (---) show pore space anisotropy. (b) This example reveals a simulated porosity of only 25%, despite a qualitative similarity with the images in Fig. 12 b, with a simulated porosity of 35.7%. To compare, the analytical porosities for samples 3 (a) and 6 (b) were ≈ 12-15 porosity % higher. The autocorrelation functions R_x (—) and R_y (---) reveal low pore space anisotropy

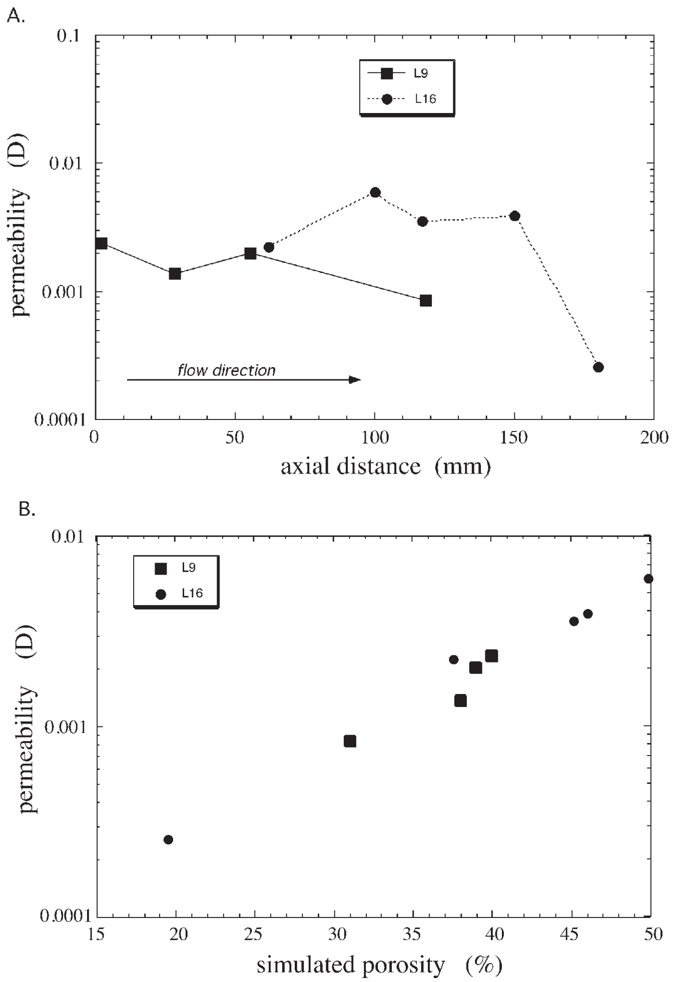

Fig. 14. (a) Simulated permeabilities along the central axes of L9-11 and L16 were derived using a reconstructed porous media method (Adler et al., 1990). Axial distance increases with direction of flow. The non-linear trend of L16 follows as a consequence of the irregular nature of the simulated porosities. (b) Simulated permeabilities as a function of simulated porosities for both L9-11 and L16 follow the same linear trend. Note that the permeabilities of L16 in particular are subject to error, given the uncertainties in the simulated porosities.

12a). The porosity of the 2000x binarized image is 35.7%. This simulated "microporosity" is in very good agreement with the measured porosities for sample no. 4 (35.1% by Hg injection and 37.6% by density technique). The autocorrelation functions R_x and R_y in both Figs. 12a and b are almost equivalent, indicating that the pore spaces show no preferred orientation.

Figure 13a shows a SEM image and its binarized equivalent for sample 3, L9-11 (see Fig. 4). This pair of images shows the sensitivity of simulated porosities to the presence of heterogeneities, in this case, a large object. The effect is dramatic, the porosity is reduced to 28%, which is much lower than the measured values of 40.6% and 43.0% (Hg injection and density methods, respectively). In the same figure the autocorrelation functions reflect a degree of anisotropy with respect to the pore spaces; this is most probably due to the influence of the large object at the top of the image. Figure 13b shows a set of SEM/binarized images (sample 6, L9-11, see Fig. 4) with a very low simulated porosity of only 25%. In comparison, the measured porosity values are significantly higher for sample 6: 41.0% and 44.0% by the Hg injection and density methods, respectively. Despite the presence of some medium-sized grains in

Fig. 13b, it is surprising that the porosity is significantly lower than that shown in Fig. 12b. The reason for the lower simulated porosity is most probably due to small pore spaces remaining unresolved during binarization of the SEM image.

Using the method of reconstructed porous media (Adler et al., 1990), the permeabilities of deformed chalk were calculated, based on the simulated porosities discussed above (using only 2000x images). The permeabilities for experiments L9-11 (samples 1, 2, 3, 5) and L16 (samples 18, 28, 33, 43, 53) as a function of axial distance and simulated porosity are shown in Figs. 14a, b, respectively. In Figure 14a, the (log) permeabilities show a general decrease as a function of axial distance; the non-linearity of the trends follows as a consequence of the irregular nature of the simulated porosity vs. distance profiles (especially expt. L16, see Fig. 11a). Figure 14b shows that the log permeability vs. porosity data for L9-11 and L16 are linear.

In analyzing the permeability relationships illustrated in Fig. 14, it is important to bear in mind that these simulated permeability estimates are subject to large errors, given the discrepancies between the simulated and the measured porosities (i.e., refer to Fig. 11a) and the fact that the permeability varies as the square of the correlation length, which is a function of the pore space diameters. Therefore, a small change in porosity translates to a large change in permeability. This has been observed experimentally with North Sea chalks, where measured permeabilities decrease sharply with increasing confining pressure (P > 8 MPa; Da Silva et al., 1985).

It is interesting to compare these simulated permeabilities with those for natural samples determined analytically. Permeabilities measured in natural chalk samples are approximately of the same order of magnitude. As an example, the permeabilities of Lixhe chalk (> 40% porosity, quarried close to Guerville chalk) are on the order of ≈ 1 mD (Schroeder et al., 1998). Similarly, chalk cores from the North Sea oil fields have permeabilities ranging from ≈ 1-7 mD (Monjoie et al., 1990).

3.4. X-Ray Computerized Tomography

In the present study, the x-ray density in the CT scans has been represented in terms of a gray scale tonality, such that high-density objects appear white and low-density objects appear black. The white rims associated with the CT images are an artifact of the technique. In order to better evaluate the post-deformation tomography images of experiments L9-11 and L16, the images obtained for an undeformed (reference) chalk sample are described first. The

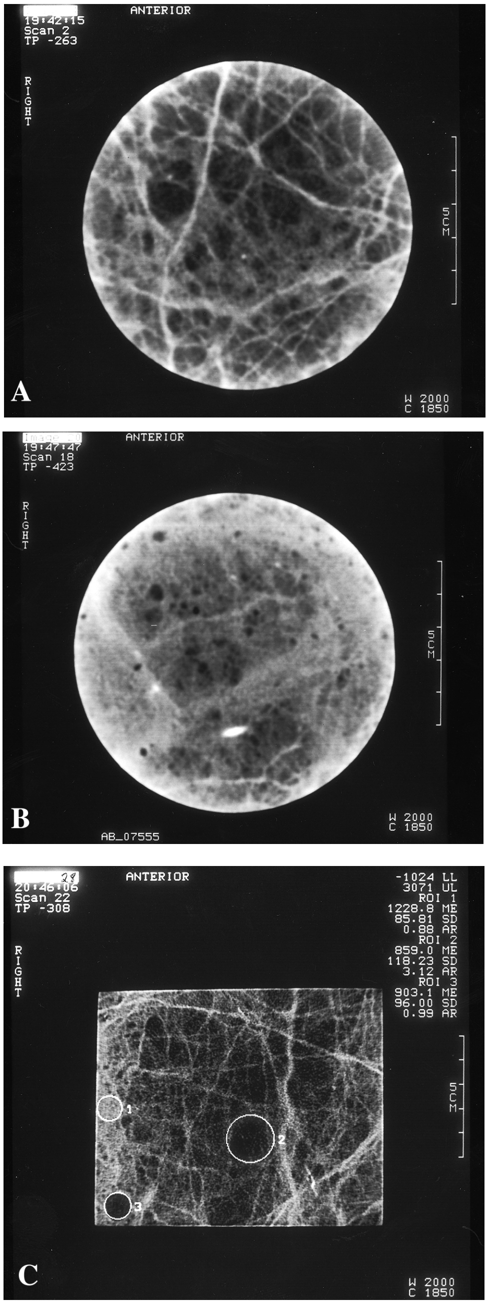

Fig. 15. X-ray computerized tomography (CT) images of an undeformed, reference sample. High and low radiological density regions are portrayed in white and black, respectively. The top and middle figures show radial images representing the far right-hand (a) and far left-hand side (b) of the axial image shown in (c). Because the samples are almost entirely composed of calcite, the radiological density can be qualitatively interpreted in terms of porosity. All images show the heterogeneous nature of the chalk, especially notable are the system of cross-cutting veins and the black "worm hole channels."

structures discussed with respect to the reference are either primary sedimentary and/or diagenetic features, or secondary in situ dissolution/precipitation features.

3.4.1. Reference sample

Sequential radial images of the reference core show that the original spatial density of the chalk is very heterogeneous, which supports the SEM observations discussed previously. Two representative radial images and an axial image are shown in Figs. 15a-c, respectively. The image in Fig. 15a corresponds to a radial slice on the far right-hand side of the axial image (Fig. 15c), whereas Fig. 15b is from the far left-hand side. All of the images display internal structures with large radiological density variations. In Fig. 15c, for example, 3 selected areas reveal large differences in density (expressed in terms of mean Hounsfield units: ME), ranging from 1229 ME (area no. 1, which shows an area of high vein density) to 859 ME (area no. 2), which corresponds to a dark region of low density. Note that the two radial images show a difference in overall density of the matrix, as evidenced by the slightly lighter color of the matrix in Fig. 15b; the lighter color translates qualitatively to a reduced porosity and more compact structure than that in Fig. 15a.

Both radial images contain numerous dark, circular to oblong-shaped regions, which are perhaps more visible in Fig. 15b, due to the lighter matrix tone. When closely comparing Figs. 15a and b, it appears that the spatial density and distribution of these regions is more or less the same throughout the reference. These dark regions have variable dimensions (up to ≈ 1 cm in diameter), and appear to be randomly distributed in all of the images; the smallest of these may correspond to the very large channels seen in SEM images- see Fig. 2. These zones appear to be spatially isolated entities since they are not sequentially continuous over more than 1 or 2 radial slices (slice separation = 7 mm). Note that in Fig. 15c, there is no evidence for single, long tubes of low porosity. Nonetheless, some of the channels may be oblique to the slices, thereby masking their connectivity. These dark, low density regions or channels resemble very closely dissolution features (often called "worm holes") created by acid percolation in limestones (e.g., see CT images of worm holes in Bazin et al., 1996). This suggests that these zones are due to dissolution, which results in the formation of short, circular to tubular zones of elevated porosity. In the study by Bazin et al. (1996), the continuity of the worm holes was a function of the rate of fluid flow; high flow rates favored single, continuous worm holes, whereas slow flow rates favored multiple-branching worm holes. Thus, the lack of single, continuous worm holes in the present study (reference and deformed samples) suggests that flow rates were slow enough to promote branching. If channel branching did occur, then some form of connectivity between some of the vertical channels cannot be excluded.

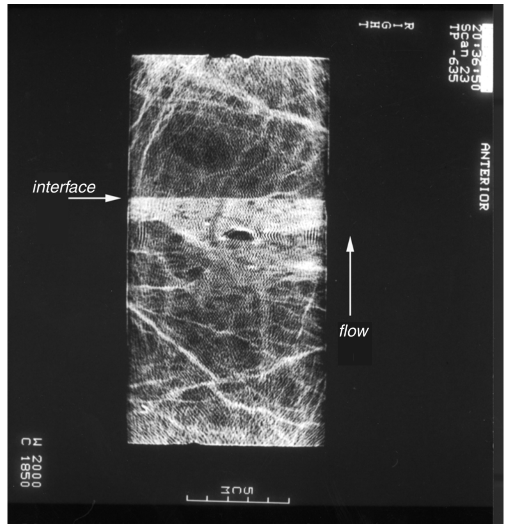

Fig. 16. Axial CT image of L9-11 after deformation. The most notable feature is a region of high density/low porosity adjacent and upstream of the interface between the two cores. The exact location of the interface is defined by the sharp and linear density contrast. The low porosity, tabular region may be the result of precipitation that occurred during deformation- see text for details.

Equally ubiquitous is the system of veins, which cross cut all of the radial and axial images of the reference. As opposed to the dark round zones, the veins show a certain degree of continuity from one radial image to the next. Note how the system of veins is more prominent in Fig. 15a vs. b; this is simply a function of a higher density contrast due to a less dense matrix (i.e., higher porosity matrix) in the former image.

3.4.2. Deformed samples

CT images of deformed chalks are shown in Figs. 16-19. The comments about channels (worm holes) discussed immediately above also apply to all of the deformed samples. A *possible* redistribution of mass due to pressure solution deformation and precipitation can be noted in an axial CT image of sample L9-11, shown in Fig. 16. In this image, fluids percolated from bottom to top in the vertically-oriented core. The most

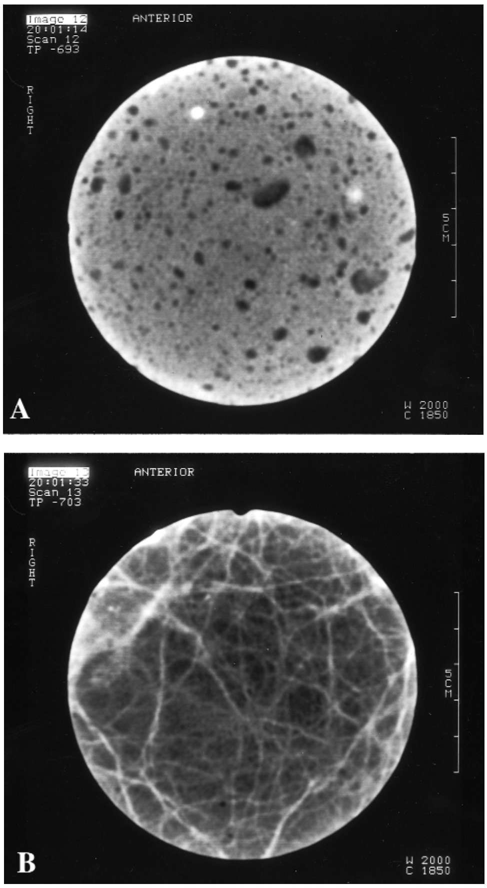

Fig. 17. Radial CT images of L9-11 after deformation, representing the interfacial area between the 2 cores. (a) CT image directly adjacent to the interface, on the upstream side (see Fig. 16). The high porosity, dark circular objects probably represent dissolution features; their connectivity is difficult to determine, however. (b) CT image directly adjacent to the interface, on the downstream side (see Fig. 16). The majority of radial CT slices, in both cores of L9-11, bear a strong resemblance to this image.

notable feature is a tabular, ≈1-1.5 cm-thick low porosity zone that occurs exclusively in the upstream core, and is perpendicular to the core axis and fluid flow direction. The sharp, linear contrast in density delimits the interface between the two cores.

Sequential radial CT images of the entire L9-11 core were also realized, with a 1-cm interval. This sequence of radial images displays a sudden change in density (and porosity) that correlates exactly to that shown in the axial image. Figures 17a, b show adjacent (1-cm separation) core slices on opposite sides of the interface, the upstream slice (Fig. 17a) is within the high-density, low-porosity zone; Fig. 17b represents the adjacent downstream slice with lower density and higher porosity. A comparison of Figs. 17a and b reveals an apparently higher density of worm holes in the region of low porosity, shown in the former image. The regions of higher density evident in Figs. 16 and 17a may correspond to low porosity cemented regions that were evidenced by SEM, as shown in Fig. 3c. The matrix shown in Fig. 17b (downstream core) is very much like that found in the majority of the upstream core, to the right (upstream) of the high-density zone shown in Fig. 16.

CT images of L16 show that this core displays roughly the same heterogeneous density variations associated with cross-cutting veins and dark, circular to oblong-shaped, low density regions as are present in L9-11. Figure 18 shows two axial images; fluid flow was from bottom to top. The interface between the two parts of the core is easily discernable in terms of a density difference; the downstream core is interpreted to have a higher porosity adjacent to the interface of the two cores. On the other side of the interface (upstream side) is a lenticular region characterized by matrix of higher density and lower porosity (Fig. 18a). The same region in Fig. 18b has a far more regular, tabular geometry. The density contrast of this region with respect to the surrounding matrix is simi-

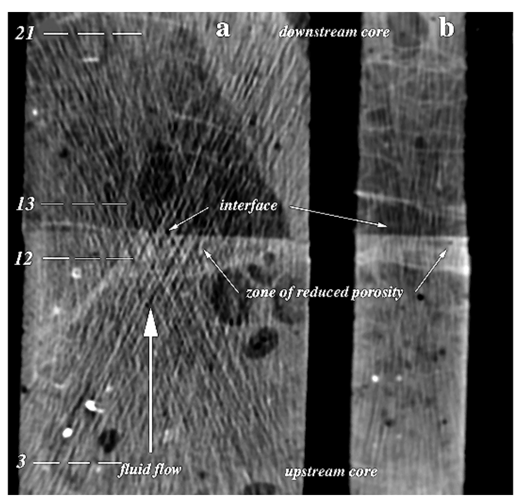

Fig. 18. Axial CT images of L16 after deformation; the interface between the cores is indicated. Image (a) is close to the axis center, image (b) is far off-center (hence the reduced thickness). Both (a) and (b) are characterized by a high density/low porosity region in the upstream core, adjacent to the interface (compare to Fig. 16). The thick diagonal band in the downstream core (image a) is interpreted to be a primary sedimentary feature; the faint diagonal bands in both images are an artifact. Nos. 3, 12, 13, and 21 (image a) refer to the locations of the radial slices shown in Fig. 19.

A.

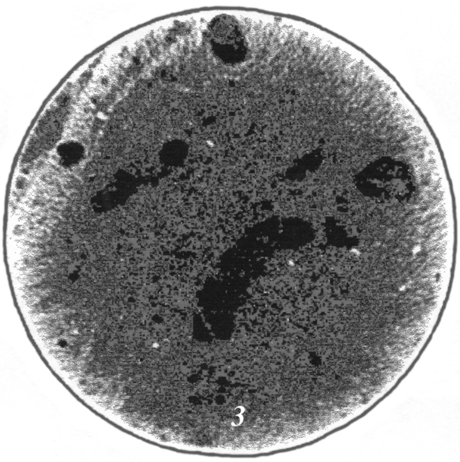

D.

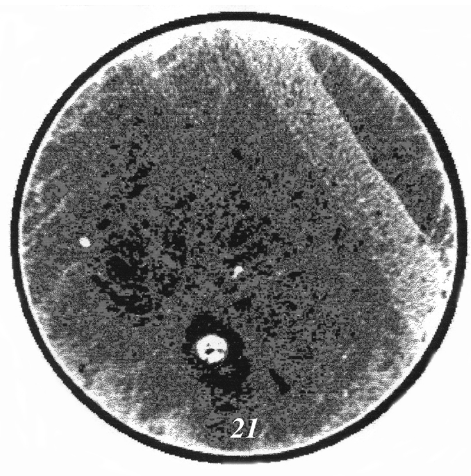

Fig. 19. Sequential radial CT images ($\phi = 10$ cm) of L16 after image treatment (positions of slices 3, 12, 13, and 21 (a, b, c, d, respectively) shown in Fig. 18a). The relative amount of "intermediate porosity" (shown by medium gray tone) decreases sharply immediately adjacent and upstream of the interface (slice 12, image b), which is in accord with the axial image shown in Fig. 18. This is interpreted to be a result of precipitation in pore spaces during deformation.

B.

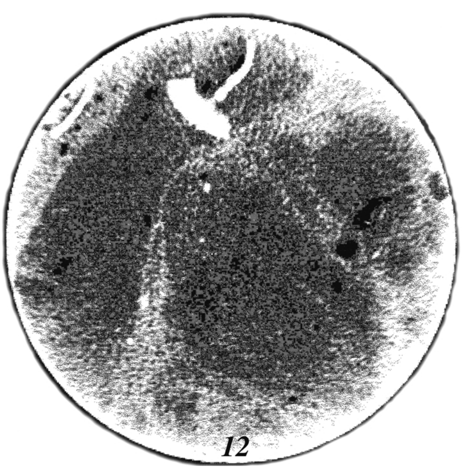

C.

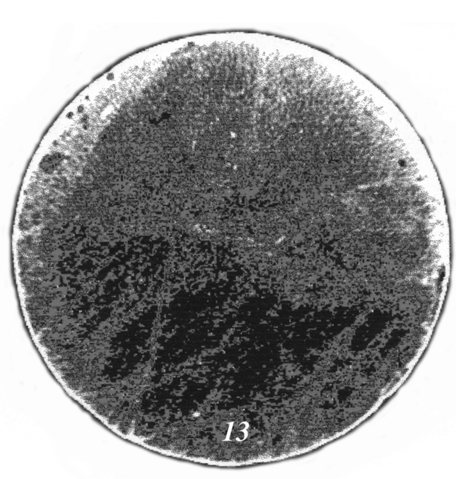

lar to the density contrast described for L9-11; in addition, the general geometry with respect to the interface, the dimensions, and the irregular nature of this region are similar to that in L9-11 (compare with Fig. 16). The downstream core also contains a high-density region (but much larger), in the form of a continuous diagonal band (Fig. 18a). This diagonal band appears in nearly all radial slices of the downstream core. The band's diagonal orientation to the fluid flow direction, its large size, as well as its sharp boundaries (i.e., on both edges-see radial slice 21 in Fig. 19) strongly suggest that this feature is a syn-sedimentary feature, and is most probably not attributable to fluid percolation, deformation, and mass redistribution within the chalk core.

In order to further investigate the spatial density variations associated with L16, 21 sequential radial tomographic images (1 cm-interval along core axis) were analyzed with image treatment software (NIH Image, release 1.61). Each radial tomography image was converted into a selective density slice, where each slice was defined by the same gray-scale density interval. The grayscale interval defines a constant interval or range of densities for any given image; the interval (which is user-adjustable) was chosen to be representative of an 'intermediate' chalk matrix density, such that high-density objects (chert fragments, veins, and bands unrelated to deformation) and low-density objects (dark, circular to oblong regions)

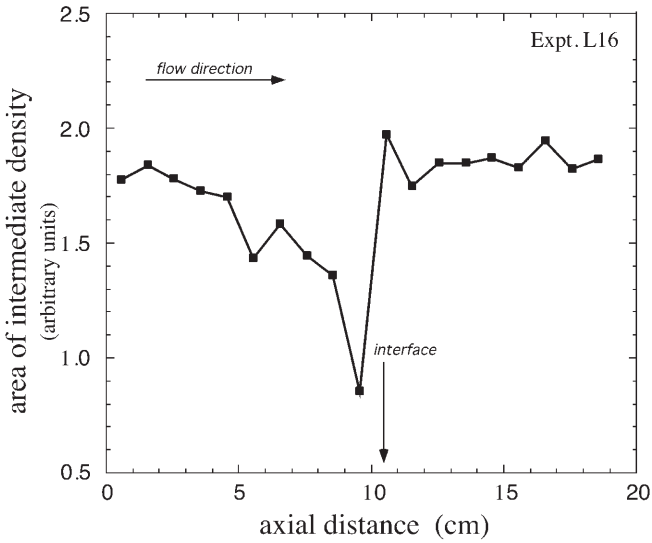

Fig. 20. Axial profile of 'intermediate' porosity of L16 (see caption Fig. 19). The decrease in 'intermediate' porosity as a function of flow direction in the upstream core is similar to overall porosity trends shown for L9-11 (all measurements) and L16 (water saturation method).

were excluded from the selective density area determinations. Figure 19 shows a sequential series of 4 selective density slices, starting from the inflow end of the upstream core (no. 3) and ending at the outflow end (no. 21) of the downstream core (i.e., bottom to top on axial image, Fig. 18a); the gray-scale density interval used for image analysis corresponds to the areas of intermediate gray tone visible in each slice. The amount of intermediate density matrix decreases significantly in slice 12; this slice corresponds to the region of high density, low porosity adjacent to the interface between the two cores (see axial image in Fig. 18). A profile representing the amount of the intermediate density (i.e., intermediate gray tone pixels of each slice) as a function of axial length is shown in Fig. 20. This profile, which should be interpreted only in a qualitative sense, shows a sharp minimum at the axial position corresponding to the upstream side of the interface between the two cores. This minimum corresponds to a sharp decrease in the area associated with 'intermediate' matrix porosity; this is interpreted to be due to a decrease of the overall porosity of the matrix by precipitation of material in pore spaces close to the interface.

Since it was not possible to obtain CT scans of each core before deformation, it is difficult, if not impossible, to positively ascribe each of the high-density/low-porosity features observed in the CT scans of L9-11 and L16 to processes of mass redistribution and precipitation that occurred as a consequence of pressure solution deformation. One can, for example, take the position that the high-density/low-porosity regions in L9-11 and L16 were already present before deformation. In support of this argument is the qualitative similarity between these regions and the high-density/low-porosity region of the reference (left-hand side of axial image, Fig. 15c). To counter this argument, it is rather improbable (but not impossible) that pre-existing high-density/low-porosity regions in L9-11 and L16 should always occur adjacent and parallel to the artificially-created boundary of the two cores, and always perpendicular and upstream with respect to the fluid flow direction. The high-density/low-porosity region of L9-11, in particular, appears to be more uniform than that in the reference, this supporting the idea of syn-deformational mass redistribution and uniform precipitation in pore spaces. It can also be noted that the upstream boundaries of the high-density regions in L9-11 and L16 are sharp, whereas in the reference, this region is diffuse and vein-like. This also supports the idea that the high-density regions in the reference and those in L9-11 and L16 were formed by different processes. Of course, it is also possible that the high-density/low-porosity regions of L9-11 and L16 started out as porosity regions with an elevated density/low porosity (e.g., left-hand side of axial image, Fig. 15c), and that precipitation was localized in these areas, such that during deformation the already present heterogeneities were accentuated. The various scenarios proposed above, unfortunately, cannot easily be resolved based solely on the data in the present study.

4. CONCLUSIONS

An important goal of this study was an investigation into how a porous material such as chalk compacts as a function of pressure solution deformation. The porosities of several reference samples (non-deformed), as well as post-deformation samples from experiments L9-11 and L16, were extensively measured in order to document the changes in porosity due to compaction. Radiological density measurements (CT scans) provided complementary information concerning density and porosity variations in a reference sample, as well as L9-11 and L16. As was discussed in detail in section *3.4.*, the interpretation of the post-deformation data is difficult because of the initial heterogeneous nature of the chalk. The ambiguities associated with the interpretation of the data make it difficult to resolve one of the key aspects of the pressure solution process - the redistribution of mass associated with compaction and precipitation in pore spaces. It is relatively certain that the primary deformation mechanism observed in the present experiments is pressure solution creep (as discussed in detail in Part 1). An important question that must be asked is what happened to the dissolved material that was removed from stressed intergranular regions?

It is evident that the process of mass redistribution, from stressed intergranular boundaries to pore spaces, is not simple. The precipitation of dissolved material can theoretically take place in the adjacent pore spaces. Many studies have documented grain overgrowths that have been interpreted to result from precipitation within the context of the pressure solution process (e.g., Dewers and Hajash, 1995). The provenance of grain overgrowth precipitates is not always clear, unless however, the pore spaces are completely unconnected, such that dissolved material can only precipitate in adjacent pore spaces. The SEM images in the present study do not show any obvious individual grain overgrowths, even though it is possible that precipitation occurred at a sub-micron scale and was therefore not observed. On the other hand, many regions containing cemented grains on the order of 10 μm in size were observed by SEM (see Fig. 3c). While such regions also were observed in undeformed chalk samples (see vein in Fig. 1b), the frequency of occurrence was higher in deformed samples, and was most notably evident in the upstream area adjacent to the two-core interface of L9-11. This area corresponds exactly to the region of high-density and low-porosity that was observed in the CT scans (Fig. 16) and measured analytically by various porosity techniques. Thus, it is very likely that the redistribution of mass in the chalk samples occurred by a deposition process that resulted in a precipitation front, producing large-scale cementation of grains. Taking chalks in the Mons basin as a comparative example, the localization of calcium carbonate precipitation, in the form of overgrowths and cemented grains, immediately adjacent to fault zones is evidence that mass redistribution associated with pressure solution deformation can be very localized in natural systems (Gaviglio et al., 1993, 1997). On a more general scale, the presence of precipitation fronts is a commonly observed geochemical phenomenon; this type of behavior has been shown to be associated with many types of ore deposits, for example.

If the high-density/low-porosity zones in L9-11 and L16 are interpreted to be due to precipitation-mass redistribution associated with pressure solution creep of chalk, then it is possible that the presence of a continuous void space, such as was present at the interfaces of the two cores in L9-11 and L16, controlled in some manner the localization of preferential precipitation. A possible change in the hydrodynamic behavior and/or a decrease in the pore pressure of the saturated solution upon entering such void regions may have had an effect on the precipitation kinetics of calcite. The onset of precipitation may in turn have favored continuous precipitation upstream from the initial regions of precipitation, thereby resulting in thick and tabular low-porosity regions. The occurrence of tabular low-porosity regions, due to uniform precipitation within the matrix, is also in accord with results from numerical models (e.g., Sallès et al., 1993; Békri et al., 1995, 1997; Mourzenko et al., 1996), based on the hydrodynamics of fluid flow, diffusivity, and kinetic rate parameters (see section *4.3.3*, Part 1 for details).

There are naturally occurring cases that may be analogous to what was observed in the present study; two examples are given. In the first example, Dunnington (1967) noted that stylolites tend to start in regions that originally have a higher degree of porosity. The formation of stylolites and the concomitant transfer and precipitation of dissolved material in turn results in regions with decreased porosity, adjacent to the higher porosity zones. Using the Mons chalk study by Gaviglio et al. (1993) as the second example, porosity reduction and cementation of grains occurred predominantly and immediately adjacent to the normal fault plane (i.e., on both sides of fault plane). It is hypothesized that fluid flow occurred from the surrounding chalk matrix to the fault planes, given that the fluid pressure in the matrix was probably higher than within the fault plane. In both of these examples, it appears that pressure solution is favored in areas or along planes that originally had a higher degree of porosity than the surrounding rock. The higher porosity zones were a locus for pressure solution, and the surrounding areas of lower porosity were the locus of local precipitation of the dissolved material.

The type of scenario described above correlates with theoretical self-organizing systems that operate on a positive feedback system (e.g., Merino et al., 1983; Merino, 1992; for a general overview, see Ortoleva, 1994). The central idea is that the inherent stress-strain energy of grain aggregates is a function of texture or porosity. Areas of slightly higher porosity (such as bedding planes, fault planes, or in the present case, the interface between the two cores) have a higher average stress-strain energy, and this causes preferential dissolution to become localized there at an accelerating rate. In a similar manner, areas of slightly lower porosity have less stress-strain energy, and thus are more likely to be a locus of precipitation. The overall result is that local porosity fluctuations tend to be amplified with time because of a positive feedback relationship that exists between porosity and preferential dissolution and precipitation. An additional factor that can be considered is the possibility that regions or zones of local precipitation behave in a more brittle manner during deformation as compared to the surrounding matrix (i.e., core interfacial regions in L9-11 and L16). The development of fractures, as a result of brittle behavior, is thought to be responsible for increasing diffusional transfer of material during deformation, thus amplifying the efficacy of pressure solution (see Gratier et al., 1999). A positive feedback process, which includes all of the factors described above, is a plausible explanation for the porosity profiles that developed during the deformation chalk, as exemplified by experiments L9-11 and L16.

Acknowledgements—This research was supported by generous grants from Elf Aquitaine (Pau, France) and the GdR-Géomécanique program (CNRS). The assistance of F. Verhelst, A. Timmerman, and K. Vandersteen (all from K.U. Leuven, Belgium) in obtaining the CT images is gratefully acknowledged. Comments from M. Jessell, C. Schroeder, F. Renard, and A.-M. Boullier aided in clarifying certain points in the original manuscript. P. Gaviglio acknowledges assistance from M. Boué in the preparation of samples. We thank Brian Evans, Enrico Merino, and Andrew Hajash for their constructive reviews of the manuscript (note: the original reviews were based on a single manuscript, before it was divided into Parts 1 and 2; however, the scientific content and interpretations remain unchanged). R.H. also thanks Brian Evans for assuming the task of editorial handling.

Finally, I would like to acknowledge David Crerar's role as teacher, advisor, and friend during the 6 years of my graduate studies in his geochemistry group in the Department of Geology and Geophysics, Princeton University. -Roland Hellmann

Editorial handling: Brian Evans

REFERENCES

Adler P. M. (1994) The method of reconstructed porous media. *Current Topics Phys. Fluids* **1**, 277-306.

Adler P. M., Jacquin C. G., and Quiblier J. A. (1990) Flow in simulated porous media. *Int. J. Multiphase Flow* **16**, 691-712.

Adler P. M., Jacquin C. G., and Thovert J.-F. (1992) The formation factor of reconstructed porous media. *Water Resources Res.* **28**, 1571-1576.

Bathurst R. G. C. (1995) Burial diagenesis of limestones under simple overburden. Stylolites, cementation, and feedback. *Bull. Soc. géol. France* **166**, 181-192.

Bayly B. (1987) Nonhydrostatic thermodynamics in deforming rocks. *Can. J. Earth Sci.* **24**, 572-579.

Bazin B., Bieber M. T., Roque C., and Boutéca M. (1996) Improvement in the characterization of the acid wormholing by "in-situ" X-ray CT visualizations, SPE Paper 31073. *International Symposium on Formation Damage Control*, Lafayette, Louisiana, U.S.A.

Békri S., Thovert J. F., and Adler P. M. (1995) Dissolution of porous media. *Chem. Eng. Sci.* **50**, 2765-2791.

Békri S., Thovert J.-F., and Adler P. M. (1997) Dissolution and deposition in fractures. *Eng. Geol.* **48**, 283-308.

Brace W. F. (1972) Pore pressure in geophysics. In *Flow and Fracture of Rocks, Geophys. Monogr. Ser.* Vol. 16 (eds. H. C. Heard, I. Y. Borg, N. L. Carter, and C. B. Rayleigh). AGU, Washington, D.C., pp. 265-273.

Brantley S. L., Evans B., Hickman S. H., and Crerar D. A. (1990) Healing of microcracks in quartz: implication for fluid flow. *Geology* **18**, 136-139.

Brown M. A., Brown M., Carlson W. D., and Denison C. (1999) Topology of syntectonic melt-flow networks in the deep crust: Inferences from three-dimensional images of leucosome geometry in migmatites. *Amer. Mineral.* **84**, 1793-1818.

Da Silva F., Monjoie A., Debande G., Schroeder C., Poot B., Detiege C., and Halleux L. (1985) Mechanical behaviour of chalks. *2nd North Sea Chalk Symposium*. Stavanger, Norway, **2**, 1-10.

de Meer S. and Spiers C. J. (1995) Creep of wet gypsum aggregates under hydrostatic loading conditions. *Tectonophysics* **245**, 171-183.

de Meer S. and Spiers C. J. (1997) Uniaxial compaction creep of wet gypsum aggregates. *J. Geophys. Res.* **102, no. B1**, 875-891.

Dewers T. and Hajash A. (1995) Rate laws for water-assisted compaction and stress-induced water-rock interaction in sandstones. *J. Geophys.Res.* **100, no. B7**, 13093-13112.

Dewers T. and Ortoleva P. (1990) A coupled reaction/transport/mechanical model for intergranular pressure solution, stylolites, and differential compaction and cementation in clean sandstones. *Geochim. Cosmochim. Acta* **54**, 1609-1625.

Dunnington H. V. (1967) Aspects of diagenesis and shape change in stylolitic limestone reservoirs. *Seventh World Petroleum Congress*, 339-352.

Evans B., Bernabé Y., and Zhu W. (1999) Evolution of pore structure and permeability of rocks in laboratory experiments. In *Growth, Dissolution and Pattern Formation in Geosystems* (eds. B. Jamtveit and P. Meakin). Kluwer Academic Publishers, Dordrecht. pp. 327-344.

Gaviglio P., d'Albissin M. C., Bergerat F., and Vandycke S. (1993) Modifications de texture dans la craie au contact de failles normales: un exemple de graben dans le basin de Mons (Belgique). *Bull. Soc. géol. France* **164**, 565-575.

Gaviglio P., Adler P., Thovert J.-F., Vandycke S., Bergerat F., Bekri S., and Lestideau R. (1997) Grain-scale microstructure and physical properties of faulted chalk. *Bull. Soc. géol. France* **168**, 727-739.

Géraud Y., Mazerolle F., Raynaud S., and Lebon P. (1998) Crack location in granitic samples submitted to heating, low confining pressure and axial loading. *Geophys. J. Int.* **133**, 553-567.

Gratier J.-P. (1987) Pressure solution-deposition creep and associated tectonic differentiation in sedimentary rocks. In *Deformation of Sediments and Sedimentary Rocks No. 29* (eds. M. E. Jones and R. M. F. Preston). Geological Society, London. pp. 25-38.

Gratier J.-P. and Gamond J. F. (1990) Transition between seismic and aseismic deformation in the upper crust. In *Deformation mechanisms, rheology and tectonics* (eds. R. J. Knipe and E. H. Rutter). Geological Society of London Special Publication 54, The Geological Society, London. pp. 461-473.

Gratier J.-P. and Jenatton L. (1984) Deformation by solution-deposition, and re-equilibration of fluid inclusions in crystals depending on temperature, internal pressure and stress. *J. Struct. Geol.* **6**, 189-200.

Gratier J.-P., Chen T., and Hellmann R. (1994) Pressure solution as a mechanism for crack sealing around faults: Natural and experimental evidence. In *Proceedings of Workshop LXIII The Mechanical Involvement of Fluids in Faulting* (eds. S. Hickman, R. Sibson, and R. Bruhn). Open-file Report 94-228, U.S.G.S., Menlo Park. pp. 279-300.

Gratier J.-P., Renard F., and Labaume P. (1999) How pressure solution creep and fracturing processes interact in the upper crust to make it behave in both a brittle and viscous manner. *J. Struct. Geol.* **21**, 1189-1197.

Gray D. R. and Durney D. H. (1979) Crenulation cleavage differentiation: implication of solution-deposition processes. *J. Struct. Geol.* **1**, 73-80.

Gregg S. J. and Sing K. S. W. (1982) *Adsorption, Surface Area and Porosity*. Academic Press, San Francisco.

Groshong R. H. Jr. (1988) Low-temperture deformation mechanisms and their interpretation. *Geol. Soc. Amer. Bull.* **100**, 1329-1360.

Heard H. C. and Page L. (1982) Elastic moduli, thermal expansion and inferred permeability of two granites to 350 °C and 55 MPa. *J. Geophys. Res.* **87**, 9340-9348.

Heidug W. K. and Leroy Y. M. (1994) Geometrical evolution of stressed and curved solid-fluid phase boundaries 1. Transformation kinetics. *J. Geophys. Res.* **99**, 505-515.

Herman G. T. (1980) *Image Reconstruction from Projections: The Fundamentals of Computerized Tomography*. Academic Press, San Francisco.

Hounsfield G. N. (1973) Computerized transverse axial scanning tomography. *Brit. J. Radiol.* **46**, 1016-1022.

Joshi M. Y. (1974) A class of stochastic models for porous media. Ph.D. thesis, University of Kansas, Kansas, U.S.A.

Lemée C. and Guéguen Y. (1996) Modeling of porosity loss during compaction and cementation of sandstones. *Geology* **24**, 875-878.

Leroy Y. M. and Heidug W. K. (1994) Geometrical evolution of stressed and curved solid-fluid phase boundaries 2. Stability of cylindrical pores. *J. Geophys. Res.* **99**, 517-530.

Merino E. (1992) Self-organization in stylolites. *Amer. Scientist* **80**, 466-473.

Merino E. and Dewers T. (1998) Implications of replacement for reaction-transport modeling. *J. Hydrology* **209**, 137-146.

Merino E., Ortoleva P., and Strickholm P. (1983) Generation of evenly-spaced pressure-solution seams during (late) diagenesis: A kinetic theory. *Contrib. Mineral. Petrol.* **82**, 360-370.

Merino E., Nahon D., and Wang Y. (1993) Kinetics and mass transfer of pseudomorphic replacement: application to replacement of parent minerals and kaolinite by Al, Fe and Mn oxides during weathering. *Am. J. Sci.* **293**, 135-155.

Merino E., Wang Y., Wang Y., and Nahon D. (1994) Implications of pseudomorphic replacement for reaction-transport modeling of rocks. *Mineral. Mag.* **58A**, 599-600.

Monjoie A., Schroeder C., Prignon P., Yernaux C., Silva F. D., and Debande G. (1990) Establishment of constitutive law of chalk and long term test. *3rd North Sea Chalk Symposium.* Copenhagen, Denmark, 1-17.

Mourzenko V. V., Békri S., Thovert J.-F., and Adler P. M. (1996) Deposition in fractures. *Chem. Eng. Communications* **148-150**, 431-464.

Nahon D. and Merino E. (1997) Pseudomorphic replacement in tropical weathering: Evidence, geochemical consequences, and kinetic-rheological origin. *Am. J. Sci.* **297**, 393-417.

NIH Image, 1996, release 1.61.

Onasch C. M. (1983) Origin and significance of microstructures in sandstones of the Martinsburg formation, Maryland. *Am. J. Sci.* **283**, 936-966.

Ortoleva P. J. (1994) *Geochemical Self-Organization*. Oxford University Press, New York.

Quiblier J. A. (1984) A new three-dimensional modeling technique for studying porous media. *J. Colloid Interface Sci.* **98**, 84-102.

Raynaud S., Fabre D., Mazerolle F., Geraud Y., and Latière H. J. (1989) Analysis of the internal structure of rocks and characterization of mechanical deformation by a non-destructive method: X-ray tomodensitometry. *Tectonophys.* **159**, 149-159.

Renard F., Park A., Ortoleva P., and Gratier J.-P. (1999) An integrated model for transitional pressure solution in sandstones. *Tectonophys.* **312**, 97-115.

Reuschlé T., Trotignon L., and Gueguen Y. (1988) Pore shape evolution by solution transfer: thermodynamics and mechanics. *Geophys. J.* **95**, 535-547.

Rootare H. M. (1970) A review of mercury porosimetry. In *Advanced Experimental Techniques in Powder Metallurgy* (eds. J. S. Hirschhorn and K. H. Roll). Plenum Press, New York. pp. 225-252.

Sallès J., Thovert J. F., and Adler P. M. (1993) Deposition in porous media and clogging. *Chem. Eng. Sci.* **48**, 2839-2858.

Schroeder C., Bois A.-P., Maury V., and Hallé G. (1998) Water/chalk (or collapsible soil) interaction: Part II. Results of tests in laboratory on Lixhe chalk to calibrate water/chalk models. *Eurock '98*. Trondheim, Norway, **2**, pp. 505-514 (SPE 47587).

Smith D. L. and Evans B. (1984) Diffusional crack healing in quartz. *J. Geophys. Res.* **89**, 4125-4135.

Spiers C. J. and Brzesowsky R. H. (1993) Densification behaviour of wet granular salt: Theory versus experiment. In *Seventh Symposium on Salt* **1**. Elsevier Science Publishers, Amsterdam. pp.82-92.

Verhelst F., Vervoort A., De Bosscher P., and Marchal G. (1995) X-ray computerized tomography: determination of heterogeneities in rock samples. *8th International Congress on Rock Mechanics*. Tokyo, Japan.

Walsh J. B. (1965) The effcts of cracks on the compressibility of rock. *J. Geophys. Res.* **70**, 381-389.
Wellington S. L. and Vinegar H. J. (1987) X-ray computerized tomography. *J. Petrol. Eng.* **39**, 885-898.